Pontifícia Universidade Católica
do Rio de Janeiro

Esteban Camilo Moreno Diaz

Influence of different heat treatment conditions on the point defects of $Al_2W_3O_{12}$ and its optical and thermal properties

Dissertação de Mestrado

Dissertation presented to the Programa de Pós-Graduação em Engenharia de Materiais e de Processos Químicos e Metalúrgicos of PUC-Rio in partial fulfillment of the requirements for the degree of Mestre em Engenharia de Materiais e de Processos Químicos e Metalúrgicos.

Advisor: Prof. Bojan Marinkovic

Rio de Janeiro

October 2021

PONTIFÍCIA UNIVERSIDADE CATÓLICA
DO RIO DE JANEIRO

Esteban Camilo Moreno Diaz

Influence of different heat treatment conditions on the point defects of $Al_2W_3O_{12}$ and its optical and thermal properties

Dissertation presented to the Programa de Pós-graduação em Engenharia de Materiais e de Processos Químicos e Metalúrgicos of PUC-Rio in partial fulfillment of the requirements for the degree of Mestre em Engenharia de Materiais e de Processos Químicos e Metalúrgicos. Approved by the undersigned Examination Committee.

Prof. Bojan Marinkovic
Orientador
Departamento de Engenharia Química e de Materiais – PUC-Rio

Prof. Roberto Ribeiro de Avillez
Departamento de Engenharia Química e de Materiais – PUC-Rio

Profa. Paula Mendes Jardim
Departamento de Engenharia Metalúrgica e de Materiais – UFRJ

Rio de Janeiro, October 14th, 2021.

Esteban Camilo Moreno Diaz

Major in Chemistry Engineering by the Fundación Universidad de América University, in 2015, Bogotá, Colombia.

Bibliographic data

Moreno Diaz, Esteban Camilo

Influence of different heat treatment conditions on the point defects of $Al_2W_3O_{12}$ and its optical and thermal properties / Esteban Camilo Moreno Diaz ; advisor: Bojan Marinkovic. – 2021.

80 f. : il. color. ; 30 cm

Dissertação (mestrado)–Pontifícia Universidade Católica do Rio de Janeiro, Departamento de Engenharia Química e de Materiais, 2021.

Inclui bibliografia

1. Engenharia Química e de Materiais – Teses. 2. Expansão térmica zero ou negativa. 3. $Al_2W_3O_{12}$. 4. Vacâncias de oxigênio. 5. Propriedades térmicas. 6. Propriedades óticas. I. Marinkovic, Bojan. II. Pontifícia Universidade Católica do Rio de Janeiro. Departamento de Engenharia Química e de Materiais. III. Título.

CDD: 620.11

In memory of my grandfather.

To my parents, Lilia Diaz and Eberto Moreno.

To my sister, Alejandra and my brother Nicolas.

To my grandmother Mery Oicata.

Acknowledgments

To the Advisor, Prof. Bojan Marinkovic, for his patience, support, advice, dedication, availability, and trust throughout the development of this study.

To Prof. Marcelo da Costa (Department of Physics, PUC-Rio), for his support and advice in the analysis and measurement of the samples for XPS characterization.

To Prof. Klaus Krambrock (Department of Physics, UFMG), for his collaboration and patience in the analysis and measurement of the samples for EPR characterization.

To Prof. Waldeci Paraguassu (Department of Physics, UFPA), for his collaboration and in the analysis of the samples for the characterization of Raman spectroscopy.

To Prof. Mary Anne White and Michael Johnson for the measurement in the thermal conductivity tests.

To the Conselho Nacional de Desenvolvimento Científico e Tecnológico (CNPQ) for the master degree scholarship

This study was financed in part by the Coordenação de Aperfeiçoamento de Pessoal de Nível Superior - Brasil (CAPES) - Finance Code 001.

The US Army Research Laboratory and the NSERC to finance this project.

To my friends from our Ceramic Materials Research Group (PUC-Rio) for their total welcome. Juliana Viol and Anja Dosen for the teachings of different characterization analyses and their achievements. In particular to Andres Ceron, Lucas Almeida, Tamires Martinhão, Fábian Orozco, Thaís Mortimer, Mayara Marzano for sharing the research environment and their knowledge with me.

To my family in Brazil, especially Juan David Caicedo, Maria Guateque, Andres Ceron and Lucas Almeida for their help and their great welcome to Brazil.

To my girlfriend Elizabeth Verdugo, for her love, help, support and understanding.

To my family for their unconditional love, support and inspiration. To my parents, sister, brother, and my grandmother Mery. I am really grateful to share this step with them.

Abstract

Esteban Camilo Moreno Diaz; Marinkovic, Bojan (Advisor). **Influence of different heat treatment conditions on the point defects of $Al_2W_3O_{12}$ and its optical and thermal properties.** Rio de Janeiro, 2021. 80p. Dissertação de Mestrado - Departamento de Engenharia Química e de Materiais, Pontifícia Universidade Católica do Rio de Janeiro.

In the development of materials resistant to thermal shock, materials with negative or near zero thermal expansion have been of vital importance in recent years. The $A_2M_3O_{12}$ family of ceramics (A = trivalent cation, M = hexavalent cation) has promising characteristics to avoid thermal shock rupture, due to its atypical thermal expansion properties. Within this family is the $Al_2W_3O_{12}$ ceramic, which has unique thermal properties and this allows its use in conditions of thermal shock. However, changes in the crystal lattice caused by point defects can generate alterations in this material. $Al_2W_3O_{12}$ ceramic can contain defects such as oxygen vacancies, which affect optical, thermal and other properties. The goal of this study is to study the influence of oxygen vacancies on the properties of $Al_2W_3O_{12}$ ceramics, as well as the importance of temperature and atmosphere in the generation of oxygen vacancies. The $Al_2W_3O_{12}$ phase was exposed to two atmospheres (H_2 and Ar) at controlled temperatures: 300°C, 400°C and 500°C to generate oxygen vacancies. The ceramic obtained was characterized by X-ray power diffraction (XRPD), diffusion reflectance spectroscopy (DRS), electron paramagnetic resonance spectroscopy (EPR), Raman spectroscopy, X-ray photoelectron spectroscopy (XPS) and thermal conductivity test. The influence of oxygen vacancies on the coefficient of thermal expansion and thermal conductivity in calcined samples in non-oxidizing atmospheres was demonstrated. Samples calcined at 500°C revealed high absorption of the ultraviolet and visible spectra compared to the samples calcined 300°C and 400°C. In addition, different states of reduced valence of W were found (such as W^{5+} and W^{4+}), through the XPS technique, in order to compensate of oxygen vacancies, that were confirmed by EPR and Raman analysis.

Keywords

Low thermal expansion; $Al_2W_3O_{12}$; Oxygen vacancies; Thermal proprieties; Optical proprieties; Charge compesation mechanism.

Resumo

Esteban Camilo Moreno Diaz; Marinkovic, Bojan (Advisor). **Influência de diferentes condições de tratamentos térmicos sobre os defeitos pontuais do $Al_2W_3O_{12}$ e suas propriedades óticas e térmicas.** Rio de Janeiro, 2021. 80p. Dissertação de Mestrado - Departamento de Engenharia Química e de Materiais, Pontifícia Universidade Católica do Rio de Janeiro.

No desenvolvimento de materiais resistentes ao choque térmico, os materiais com expansão térmica negativa ou próxima a zero têm sido de vital importância nos últimos anos. A família de cerâmicas $A_2M_3O_{12}$ (A = cátion trivalente, M = cátion hexavalente) apresenta características promissoras para evitar a ruptura por choque térmico, devido às suas propriedades diferenciadas de expansão térmica. Contudo, mudanças na rede cristalina causadas por defeitos pontuais podem gerar alterações neste material. A cerâmica $Al_2W_3O_{12}$ pode conter defeitos como vacâncias de oxigênio, que afetam suas propriedades ópticas, térmicas e outras propriedades. O propósito deste trabalho é estudar a influência das vacâncias de oxigênio sobre as propriedades da cerâmica $Al_2W_3O_{12}$, bem como, a importância da temperatura e da atmosfera sobre a geração de vacâncias de oxigênio. A fase $Al_2W_3O_{12}$ foi exposto a duas atmosferas (H_2 e Ar) sob temperaturas controladas de 300°C, 400°C e 500 °C com o proposito de gerar vacâncias de oxigênio. A cerâmica obtida desta forma foi caracterizada por técnicas de difração de pó de raios-X (DPRX), espectroscopia por refletância de difusão (DRS), espectroscopia de ressonância paramagnética eletrônica (EPR), espectroscopia Raman, espectroscopia de fotoelétrons de raios-X (XPS) e teste de condutividade térmica. A influência das vacâncias de oxigênio no coeficiente de expansão térmica e na condutividade térmica nas amostras calcinadas em atmosferas não-oxidantes foi demonstrada. As amostras calcinadas a 500°C revelaram uma alta absorção do espectro ultravioleta e visível em relação às amostras calcinadas em 300°C e 400°C. Além disso, foram constatados diferentes estados reduzidos de valência do W (tais como W^{5+} e W^{4+}) através da tecnica de XPS a fim de compensar vacâncias de oxigênio que foram confirmadas pela analise de EPR e Raman.

Keywords

Expansão térmica zero ou negativa; $Al_2W_3O_{12;}$ Vacâncias de oxigênio; Propriedades térmicas; Propriedades óticas; Mecanismo de compensação de carga.

Content

Figure list

Table list

1
Introduction

Most solids increase volume when heated and this is known as positive thermal expansion (PTE). An explanation for this behavior is when a solid is subjected to thermal excitation, assymetric longitudinal atomic vibrations cause increase in volume. However, there are few ceramic families with negative thermal expansion (NTE) or near-zero thermal expansion (NZTE). These materials contract on heating, or almost maintain their initial volume. The phenomenon of NZTE makes the materials more resistant to thermal shock since it avoids stresses formation by temperature changes. These materials can be used in countless applications where temperature change must be taken into consideration [1] [2].

The NTE and NZTE occur in the $A_2M_3O_{12}$ ceramic family, where A can be a trivalent rare earth or transition metal, while M can be W or Mo. The $Al_2W_3O_{12}$ phase belongs to this family. Nevertheless, ceramic materials can contain specific point defects such as oxygen vacancies ($V_O^{\bullet\bullet}$, as written by Kröger-Vink notation), that affect their properties, such as electrical conductivity [3], absorption of the visible spectrum [4][5], thermal expansion and thermal conductivity [6].

Therefore, the present work aims to evaluate some of the properties above described as a function of point defects such as oxygen vacancies in $Al_2W_3O_{12}$ phase, an archetypical material from the $A_2M_3O_{12}$ ceramic family.

Thus, the present dissertation is organized as follows:

- Chapter 2: Literature review, which presents the fundamentals of thermal expansion in the $Al_2W_3O_{12}$, the potential uses and the basis in identification and formation of oxygen vacancies, and the possible consequences of oxygen vacancies formation of $Al_2W_3O_{12}$.
- Chapter 3: Objetives.
- Capítulo 4: A study of oxygen vacancies formation in $Al_2W_3O_{12}$ and characterization techniques.

- Chapter 5: Effects of oxygen vacancies formation in $Al_2W_3O_{12}$ and their influence on the physical properties, such as thermal expansion, thermal conductivity and light absorbtion.
- Chapter 6: Conclusions and future works.
- Chapter 7: Bibliography.

2
Literature review

2.1
Thermal expansion

The increase of volume of material occurs generally when temperature increases. This behavior is usually exhibited by most solids and is known as positive thermal expansion (PTE) [7].

The potential energy (U) well can be used (Figure 1) to understand the PTE. This concept relates the interatomic distance with the increase in temperature. In Figure 1, "*r"* represents the interatomic distance between two atoms bonded to each other. The bottom of the well indicates the smallest, equilibrium, interatomic distance between two atoms at 0 K. At the top of the well interatomic distance between the two atoms are higer and eventually the bonds will break.

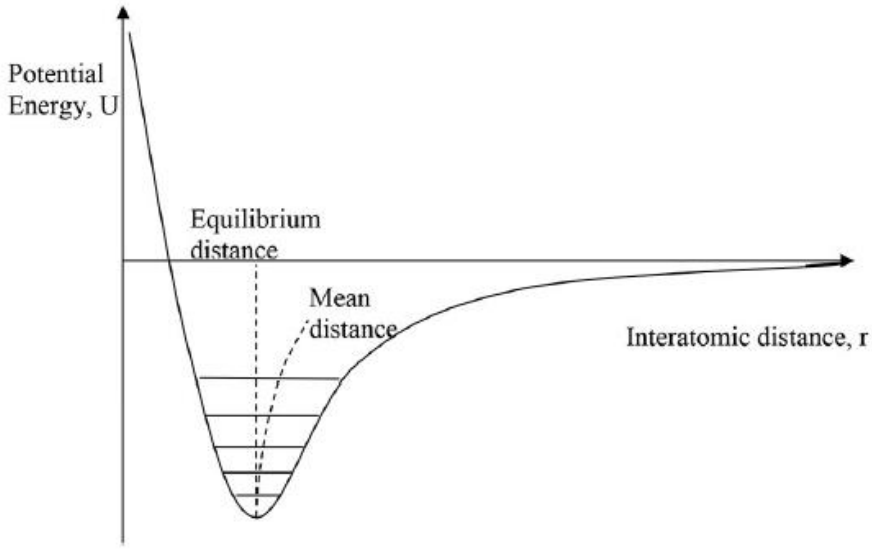

Figure 1: Relation between potential energy well and interatomic distance, showing the distance between two atoms and their kinetic energy levels. [8]

At higher vibration energies (i.e., at higher temperatures), the atoms will vibrate more in the assymetric potencial and the distances among the neigbouring atome will increase. In this way, a material will increase its volume. When the

potential energy curve is not asymmetric, the interatomic distance would not increase and, therefore, no thermal expansion would exist. When the potential energy curve is deep and narrow, the material shows a slower rate of increase in intermolecular distance leading to a lower coefficient of thermal expansion (CTE) [1][7].

However, some materials exhibit anomalous behavior when are heated. A example are thermomiotic ceramics suchs as $Al_2W_3O_{12}$. Some thermomiotic materials shows a reduction in volume or do not present significant volume changes when temperature increases, this is known as NTE or NZTE, respectively [9]. The potential energy well is unable to explain this behavior, since only the longitudinal vibrations are considered, while specific structural and vibrational features are not considered [9].

2.1.1 Coefficient of thermal expansion

In constant pressure processes, the CTE defines the change in dimension with increasing temperature. The CTE can be defined as volumetric or linear and it is represented by the Greek letter α.CTE is defined mathematically according to equations 1 and 2.

Equation 1: Volumetric coefficient of thermal expansion

$$\alpha_v = \frac{\Delta v}{v_0 \Delta T}$$

Equation 2: Coefficient of linear thermal expansion

$$\alpha_l = \frac{\Delta l}{l_0 \Delta T}$$

Where v_0 is initial volume, Δv is variation in volume, l_0 is initial length, Δl is variation in length and ΔT is the change in temperature. In anisotropic crystalline materials, different α_l values are observed for different directions. On the other

hand, in isotropic materials the relationship $\alpha_v = 3\alpha_l$ can be established and α_l is the same along all three crystallographis directions [1][7].

2.2 Mechanisms of NTE

A quantized lattice vibration in a crystal is known as a phonon and these can be longitudinal (Figure 2 a) and transverse (Figure 2 b and c)[1]. Transverse vibrations can be classified into high energy optical or low energy acoustic. Figure 2 shows a schematic representation of the vibrations experienced by large arrays of atoms in thermomiotic ceramis and these vibrations have their energy quantized by phonons [8].

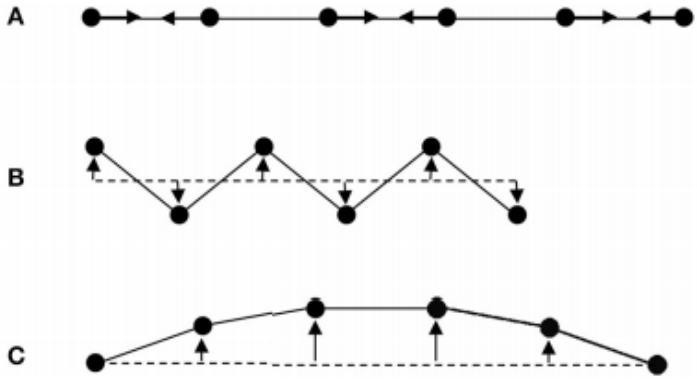

Figure 2: Schematic representation of (a) longitudinal vibrations (b) optical transverse vibrations and (c)acustic transverse vibrations [8]

Figure 3 is a schematic representation of the vibrations between two metals joined by one 2-folded oxygen linker (M-O-M). Longitudinal motions tend to lengthen the chain of connected atoms with the increase in temperature causing a PTE. Whereas, in transverse vibrations, the angle formed by the transverse movement of oxygen tends to shorten the distance between second neighbours M-M in the chain of atoms, causing a decrease in volume and therefore this can lead to NTE, if the transverse vibration contribution outweights longitudinal bond lengthening [8][10].

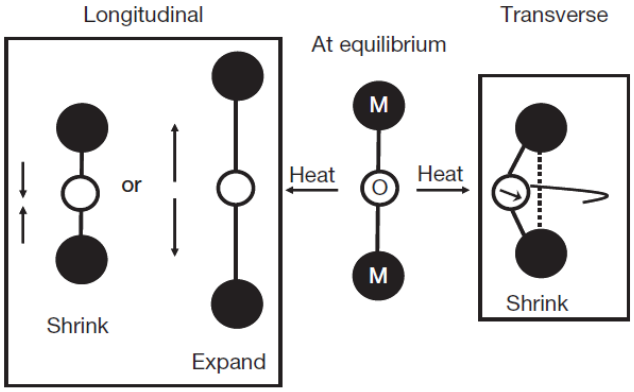

Figure 3: Longitudinal vibrations increase the interatomic distance, on the other hand, the angle formed by transverse vibrations shortens the distance between the atoms [1]**.**

Structurally, in thermomiotic ceramics, the atoms are arranged in tetrahedral and octahedral structures connected by the vertices in an open framework, low-dense, structure. Open framework structures favored the NTE generating since transverse motions not constrained by steric effect of neighbouring atomic species. Figure 4 shows an example of the orthorhombic crystal structure adopted by thermomiotic material from $A_2M_3O_{12}$ family, such as $Sc_2W_3O_{12}$ [9][7].

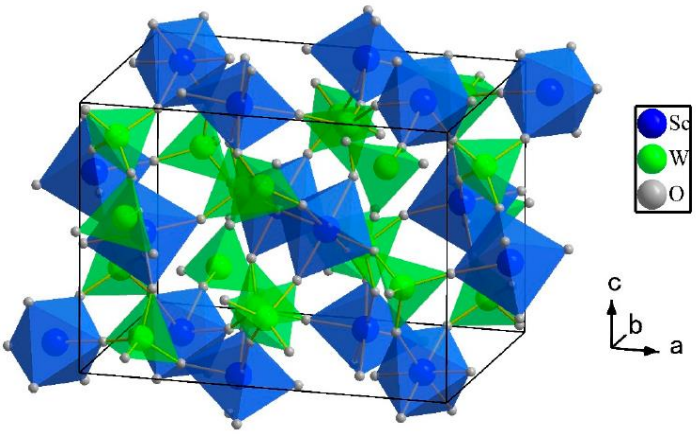

Figure 4: Orthorhombic crystal structure of $Sc_2W_3O_{12}$ belonging to the $A_2M_3O_{12}$ family of ceramic. In blue: ScO_6 octahedra, in green: WO_4 tetrahedra [9]**.**

When the crystallization process occurs, the material can adopt a monoclinic or orthorhombic structure, and a phase transition between these phases may occurs

at a specific temperature. [1] However, the low density of the orthorhombic structure facilitates the transverse movement of two-folded linkers (oxygen anions). Another characteristic of the $A_2M_3O_{12}$ family contributing to the NTE is strong M-O bonds (and in lower extent A-O bonds which contribute less to longitudinal asymmetric vibrations [7].

2.3
$Al_2W_3O_{12}$: A short overview

Ceramic families which present NTE or NZTE are: AM_2O_8, AM_2O_7, $A_2M_4O_{15}$ and $A_2M_3O_{12}$[1]. The later causes great interest due to great chemical flexibility, while keeping orthorhombic, low-density, crystal structure [9].

There is a huge number of crystalline phases inside $A_2M_3O_{12}$ family. The member A is a trivalent cation, a smaller lanthanide element or transition metal and M is W^{6+} or Mo^{6+} [9].

Coefficent of thermal expansion in orthorhombic phase depends on the size of the cation A. For example, when the atomic radius is large (1.01 Å as reported for Y^{3+}) [11] favor large channels in the structure, which allow the entry of molecules such as water inside the crystal structure. The presence of water molecules inside orthorhombic phase can reduce the contribution of transverse motions to CTE due steric hindrance and, therefore, NTE contribution may not outweighs PTE due to potential well assymetry. On the other hand, Al^{3+} with a relatively low ionic radius (0.54 Å) prevents water entance and, therefore maintain orthorhombic structure[9][12][13]. Consequently, this phase does not have its low-positive CTE affected by water molecules.

$Al_2W_3O_{12}$ is a phase that belongs to the $A_2M_3O_{12}$ family [14]. In $Al_2W_3O_{12}$, WO_4 assumes a tetrahedral structure and AlO_6 octahedral structure [15], these two polyhedra are joined by vertices through oxygen linkers forming an A-O-W bridges. Thus, $Al_2W_3O_{12}$ satisfies the conditions to present a NZTE behavior and to be a potential candidate in studies and industries where thermal expansion is important[9].

Due to the thermal properties and simple chemistry, $Al_2W_3O_{12}$ is an interesting material in thermal operations. For example, $Al_2W_3O_{12}$ is a promising material as a substitute for sapphire in infrared windows that must be resistant to

thermal shock[16]. In addition, it can be used in thermoplastic matrices as a filler to reduce their CTE. It is worth noting that high CTE of thermoplastics limits their use in the aerospace and microelectronics industries[17].

Different authors have calculated the CTE of $Al_2W_3O_{12}$. Table 1 shows the CTE values obtained in different studies. According to Jardim et al.[18], the difference in the results corresponds to errors associated with the experimental techniques used in the measurement. Table 1 indicates the contraction behavior in the *b* and *c* axes, however in the *a* axis there is a PTE behavior, demonstrating the anisotropy thermal expansion behavior for $Al_2W_3O_{12}$.

Table 1: CTE of $Al_2W_3O_{12}$ from different authors

$\alpha_a(K^{-1})$	$\alpha_b(K^{-1})$	$\alpha_c(K^{-1})$	$\alpha_l(K^{-1})$	$\alpha_v(K^{-1})$	Ref.
$5.94x10^{-6}$	$-0.099x10^{-6}$	$-1.31x10^{-6}$	$1.5x10^{-6}$	$4.51x10^{-6}$	[11]
$8.31x10^{-6}$	$-0.15x10^{-6}$	$-1.69x10^{-6}$	$2.15\ x10^{-6}$	$6.47\ x10^{-6}$	[19]
-	-	-	$1.71x10^{-6}$	-	[20]
-	-	-	$1.5x10^{-6}$	$4.51x10^{-6}$	[21]

Another application of $Al_2W_3O_{12}$ was reported by Mirsadeghi et al. [15]. They synthesized nanoparticles of $Al_2W_3O_{12}$ with a size of 40 nm for photocatalytic purposes in the reduction of *imatinib mesylate* an anticancer drug. The authors proved that $Al_2W_3O_{12}$ nanoparticles degraded this drug under UV light radiation.

Regardless of synthesis route $Al_2W_3O_{12}$ has defects and defects or changes in the original structure of $Al_2W_3O_{12}$ can modify their properties. For this reason, defects in ceramics such as $Al_2W_3O_{12}$ have attracted attention in recent years.

2.3.1 Defects in $Al_2W_3O_{12}$ and its physical properties

As the author demonstrates, there are no studies reporting the influence of point defects, such as oxygen vacancies, on $Al_2W_3O_{12}$. However, different studies have shown that through modification of the structure and composition of the material, the properties of $Al_2W_3O_{12}$ can be changed.

For example, Yanase et al.[22] studied the effect of substituting Al^{3+} for B^{3+} and observed that the color in $Al_2W_3O_{12}$ is modified by the metal doping. In another study, Dasgupta et al. [23] investigated the optical properties in $Al_{2-x}Sc_xW_3O_{12}$ as an alternative for infrared transmission window materials with low thermal expansion. They obtained a high transmittance index in the infrared spectrum and a low thermal expansion in temperature ranges between 25 and 700 ° C.

In a study by Costa et al.[21], Al^{3+} was replaced by Ga^{3+} in $Al_2W_3O_{12}$ to determine changes in thermal shock properties and due to limited solid solubility of Ga^{3+} in $Al_{2-x}Ga_xW_3O_{12}$ it was not possible form a phase with CTE close to zero. Therefore, $Al_{2-x}Ga_xW_3O_{12}$ is not a good choice as a candidate for thermal shock resistance. Recently, Ceron et al.[24] showed that in $Al_{2-x}In_xW_3O_{12}$ ceramics, substitution defects are not promising to form materials with thermal expansion close to zero.

On the other hand, there are also property changes in $Al_2W_3O_{12}$ by partial substitution of the W^{6+} cation. Surjith et al. [25] investigated cationic substitution defects in $Al_2W_3O_{12}$, by the partial substitution of W^{6+} for Mo^{6+} to determine the structural and microwave dielectric properties. Surjith et al. showed that $Al_2W_{3-x}Mo_xO_{12}$ (x=1) exhibited low dielectric constant in comparasion to $Al_2W_3O_{12}$. Also, Schulz et al. [26] observed substitution defects in $Al_2W_{3-x}Mo_xO_{12}$ to be promising for electrodes for lithium ion batteries.

Oxygen vacancies can also greatly alter the properties of a material [27][28]. The physical properties affected by Oxygen vacancies are used in a wide range of applications such as conservation of energy, fuel cells, batteries or sensitive solar cells, fields of water treatment, energy storage, and physical devices such as resistance change [29]. Until this moment, oxygen vacancies have not been studied for $Al_2W_3O_{12}$, as the author is aware of, despite their influence on physical properties.

2.4
Point defects in ceramics

There is a wide variety of defects in ceramics as shown in the figure 5, which can be classified according to their dimensions as shown in the table 2.

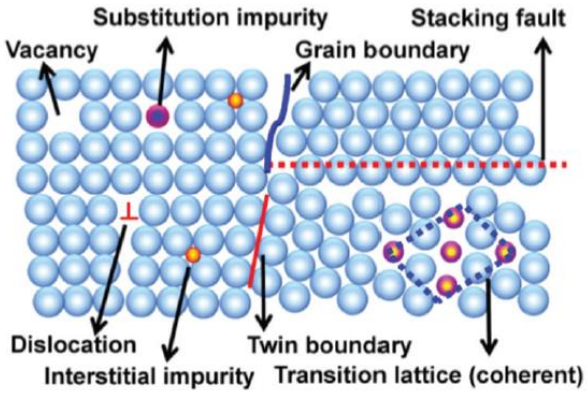

Figure 5 Schematic representation of defects in a crystal lattice[29]

Table 2: Classification of crystalline defects according to their dimensions [30]

Dimensional	Type of defect
0-dimensional	Point defects
1-dimensional	Dislocations
2-dimensional	Stacking faults, twins Grain and phase boundaries Facets
3-dimensional	Precipitates, inclusions Microvoids (vacancy agglomerates) Bubbles, dislocation clusters

Within the 0-dimensional type, a classification into intrinsic and extrinsic defects has been established. Intrinsic defects refer to an atom from the same lattice that alter the crystal lattice. On the other hand, extrinsic defects are identified by the presence of atoms that are not an original part of the crystal lattice and these are usually considered as impurities [31]. Therefore, points defects can be intrinsic and extrinsic.

Point defects in ceramics represent a deviation in the periodicity of the crystal lattice and these are considered in clasification zero-dimentional which are substitutional impurities, interstitial, ionic vacancies, Frenkel and Shottky defects [27] [30].

When an atom is removed from its site in the crystal structure and put into an interstice of the same crystal structure, a cationic vacancy is formed and it is classified as a Frenkel defect. In defects where anionic and cationic vacanciesare are created simultaneously is known as Schottky defect.

Figure 6 shows the schematic representation of Schottky and Frenkel defects. [32] [27][33].

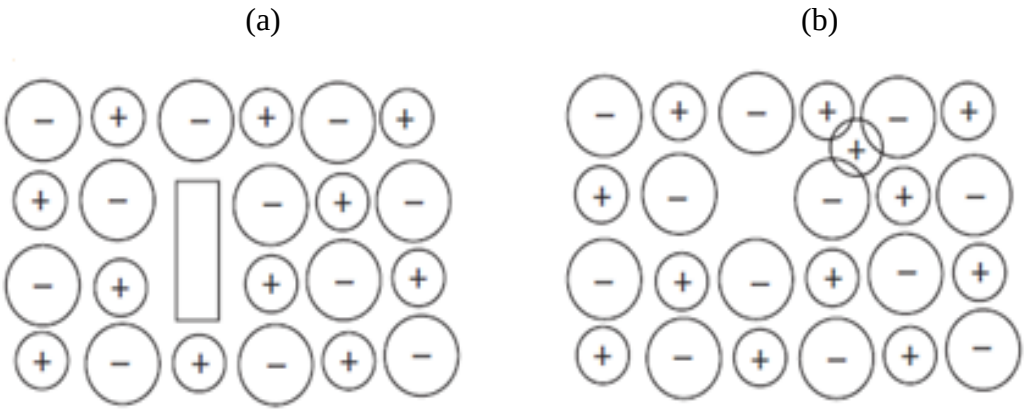

Figure 6: Schematic representation of Schottky (a) and Frenkel (b) defects [28]**.**

Point defects impacts on different physical properties such as the optical, mechanical, thermal properties, electrical, and acoustic. In addition to the alterations in the properties, vacancies are the most commonly observed defect because high temperatures in crystal synthesis strategies produce changes in atomic positions, leaving behind empty lattice sites[29].

2.4.1
Kröger-Vink notation and charge compensation

Due to the complexity and variety of point defects in ceramic materials, the Kröger-Vink notation is necessary to identify the type of defect present in these materials. The Kröger-Vink notation considers charge neutrality, mass balance and preserving the relationship of sites.

Ions can interact in the crystal lattice of ceramic materials. In a crystal, two ions of opposite charge attract each other (anion (-)–cation (+)). Whereas, two ions with the same charge will move away from each other (anion (-) –anion (-) or cation (+)-cation (+)). According to the second rule of Pauling, in the crystal structure the sum of the charges of the cations must be equal to the charge of the anions. When the second Pauling rule not satisfied, the charge neutrality is lost. Therefore, charge compensation is required to maintain charge neutrality of a crystal. For example,

the charge compensation in WO_3 for oxygen vacancies is the valence change of W^{6+} to W^{5+} or W^{4+} [4][34][35].

In the Kröger-Vink notation are considered the atom or vacancy (*S*), the crystal site ($_p$), and the charge of the defect this is called effective charge (^{C}). Efective charge can be negative ($^/$), positive ($^•$) or neutral (^{x}). The overall structure can be described as:

$$S_p^c$$

For example, an application of the Kröger-Vink notation is used in equation 3 that represents a reaction for formation of an ionized oxygen vacancy. On the left side of chemical defect reaction, atom of oxygen (*O*) at the site of oxigen ($_O$) has a neutral charge (*x*). The final expression is O_o^x. On the right side, oxygen leaves its original position in the gaseous state (½ O_2 (*g*)), a vacancy is formed (*V*) and with two positive effective charges ($^{••}$). Finally, charge neutrality is obtained with two electrons ($2e^{´}$).

Equation 3: Kröger-Vink notation for formation of an ionized oxygen vacancy.

$$O_o^x \rightarrow \frac{1}{2} O_2(g) + V_o^{••} + 2e^{´}$$

Another example of Kröger-Vink notation can be the representative of Schottky defect in a perfect crystal (null) of $Al_2W_3O_{12}$ as show in equation 4.

Equation 4: Kröger-Vink notation for Schottky defect in $Al_2W_3O_{12}$.

$$null \rightarrow 2V_{Al}^{´´´} + 3V_W^{´´´´´´} + 12\, V_o^{••}$$

2.5 Ionic vacancies

Figure 7 shows a schematic way to represent ionic vacancies in the crystal lattice. For $Al_2W_3O_{12}$, the cationic vacancies are the absence of Al or W and the

anionic vacancies are the absence of oxygen for this reason both (i.e. ionic and cation vacancies) are considerated intrinsic defects.

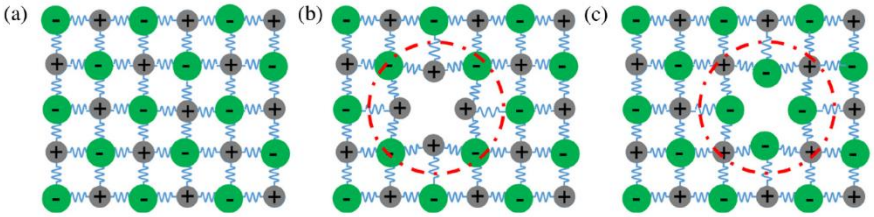

Figure 7: Schematic representation of ionic vacancies in the crystal lattice (a) crystal lattice without vacancies (b) crystal lattice with anionic vacancy (c) crystal lattice with cationic vacancy [33]**.**

When an ion is removed from its original position, it leaves behind a vacancy with some type of charge, creating states inside the band-gap. For expamle, Kotlov et al. [36] suggested the importance of the oxygen anion on the creation of free electrons and the holes in the $Al_2W_3O_{12}$. Therefore, the formation of ionic vacancies, such as oxygen vacancies, adjusts the band-gap. Besides this, ionic vacancies have an important role in different properties such as catalytic, optical, conduction, etc [27][29][37][38].

According to statistical thermodynamics the number of vacancies can be estimated with equation 4. Where N is site density and $\exp(-\Delta E_f/2kT)$ is probability of formation of Schottky pairs [29][34]. Equation 5 mathematically shows the importance of temperature in the vacancy formation process.

Equation 5: Relation between number of vacancies and temperature

$$n_s = N \exp\left(\frac{-\Delta E_f}{2kT}\right)$$

2.6
Mechanism of oxygen vacancies formation

The formation process for oxygen vacancies can be divided depending on the approach used for the formation of these point defects. The first one is related to oxygen vacancies due to cationic substitution and the second one due to anion non-stoichiometry. Regardless the approach used, reactions conditions such as temperature is considered to generate oxygen vacancies [39].

2.6.1
Oxygen vacancies due to cation substitutions

The generation of oxygen vacancies due to cation substitutions can be divided in two mechanisms. In the first mechanism, a cation at the crystal is replaced by cation with a lower valence causing formation of oxygen vacancies due to the charge neutrality requirement in the crystal cell [39]. Figure 8 is a schematic representation of the formation by this method, where the original cation is green, the cation with a lower valence is blue and the oxygen is red. For example, Mefford et al.[40] reported a study related to this method. They reported that by controlling the partial substitution of Sr^{2+} by La^{3+}, it was possible to obtain oxygen vacancies in $La_{1-x}Sr_xCoO_{3-\delta}$ system.

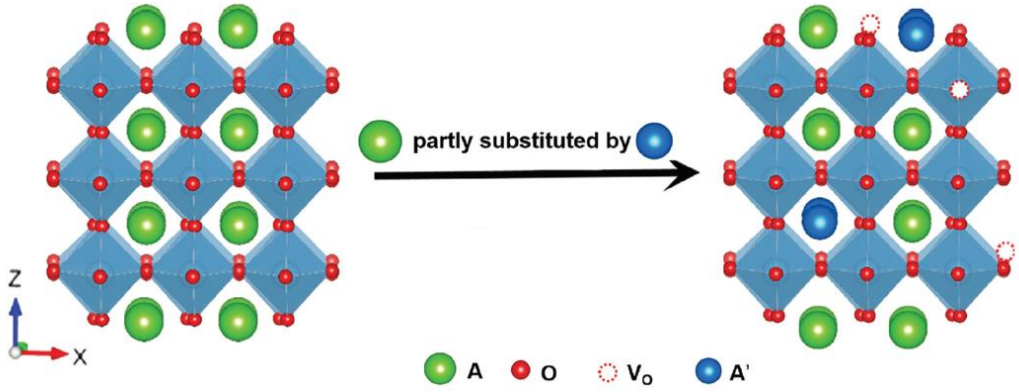

Figure 8: Schematic representation of the cationic substitution of a cation by a cation with a lower valence or a different atomic radius. Adapted by Ji et. al [39]**.**

The second way to obtain oxygen vacancies due to cation substitution is by isovalent substitution. The cation is replaced by another cation of the same valence but of a different atomic radius. Isovalent substitution generates a disorderly structure that produces the appearance of oxygen vacancies [39].

2.6.2
Oxygen vacancies due to anion non-stoichiometry

The formation of vacancies due to anion non-stoichiometry is the most traditional and simple method. It uses vacuum or atmospheres such as nitrogen, argon, hydrogen or a mixture of these. The use of hydrogen is the most common in this method.

Different authors used anion non-stoichiometry to obtain oxygen vacancies. For example, Shihao Chen et al.[41] obtained oxygen vacancies using vacuum, at 400 °C for 3 h in TiO_2. On the other hand, different concentrations of oxygen vacancies were obtained by Xia et al. [35] in WO_3-TiO_2 when exposed to hydrogen atmosphere, at 600 °C during 2 h to 9 h. In another research, Cheng et al.[5] used helium atmosphere for 5 min at 500 °C to generated oxygen vacancies in $In_{0.6}(HfMg)_{0.7}Mo_3O_{12}$. Finally, argon was used as an inert atmosphere to obtain oxygen vacancies by Ubenthiran et al.[42], within the temperature ranges between 1200 °C and 1500 °C in yttria stabilized zirconia. Therefore, to obtain oxygen vacancies in $Al_2W_3O_{12}$ reducing atmospheres, temperature and time are factors to be considered.

On the other hand, oxygen vacancies are also formed by applying a certain voltage in the material. This method is known as electrochemical reduction [37]. Wang et al. [43] used the electrochemical reduction method to obtain oxygen vacancies in WO_3. They reported color changes in the material that is an indication of oxygen vacancies formation. In this case (WO_3), oxygen vacancies were confirmed indirectly by X-ray photoelectron spectroscopy (XPS) through reduction of W^{6+} to W^{5+} to maintain the charge neutrality of the crystal.

2.7
Optical properties of ceramic materials with ionic vacancies

The relationship between optical properties and ionic vacancies in ceramic materials can be understood with band theory.

Three important concepts are considered in band theory. The valence band (VB), built from the electrons within the hignest electron orbitals. The conduction band (CB) in which the excited electrons are free to move. Finally, the bandgap is the energy difference between the VB and CB. A simple diagram of the band theory can be seen in the Figure 9 [44][28].

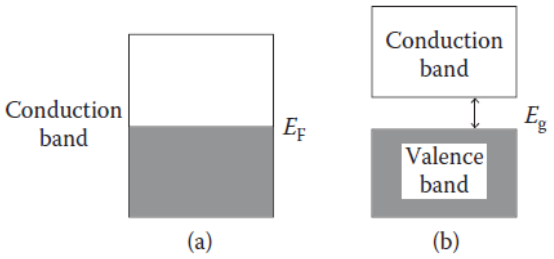

Figure 9: Schematic representation of band theory (a) conductors and (b) semiconductor such as $Al_2W_3O_{12}$ [28].

The bandgap values of ceramic or semiconductor materials can be modified by the presence of intermediate levels. The ionic vacancies form new levels near the VB and CB[45]. Anionic vacancies, such as oxygen vacancies, generate energy levels close to CB. On the other hand, cationic vacancies generate a level close to VB. Therefore, ionic vacancies have an important role in the transitions between the electronic band of the semiconductor [28][34].

The energetic distance of the levels generated between the VB and CB reduce the value of the bandgap and facilitate the increase of the absorption of the visible spectrum. Ionic vacancies can promote the absorption of visible light and alter the coloration of ceramic materials [28]. Colorless ceramic materials such as TiO_2 [46] tend to gain a dark coloration with the presence of anionic vacancies.

Optical properties such as color can be controlled with the presence of new electronic levels. When ionic vacancies are generated in ceramic materials, color centers are formed. Color of a solid is the complement the color center absorbed by the color center. When the vacancies are anionic the color centers are known as F color centers. They are due to electron or hole trapped.[34]

Yanhui et al.[47] used oxygen vacancies in Bi_2WO_6 to enhance the photocatalytic activity in this material. The improvement in the optical absorption of Bi_2WO_6 is attributed to the electrons trapped by the oxygen vacancies.

In other studies, Qi Liu et al.[4] presented color changes in WO_3 associated with the generation of oxygen vacancies. The optical properties in WO_3 were modificated because the absorption of the UV-visible spectrum is greater with the presence of oxygen vacancies.

2.8
Thermal conductivity with ionic vacancies

Another property that can be modified by oxygen vacancies is thermal conductivity. Thermal conductivity is the transfer of thermal energy from a particle to its closest particles, this can be by radiation, convection or conduction. However, in solid materials the main mode of heat transfer is thermal conduction. Thermal conductity in materials is affected by rigidity of solid, density of the crystal lattice, crystalline structure, interatomic interactions, vacancies or ionic substitutions. Figure 10 is a schematic representation of vibrational transfer between nearby atoms. [48][33]

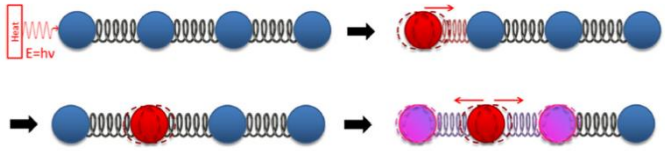

Figure 10: Schematic representation of thermal conductivity. Where the red spheres are atoms with high energy vibrations due to the thermal energy and the blue atoms are the atoms with low energy vibrations. The direction of interaction between the blue and red atoms is represented by the red arrow [48]**.**

Thermal conductivity (*k*) in ceramic materials is usually expressed in units of W (m K)$^{-1}$ and is defined by equation 6.

Equation 6: Thermal conductivity.

$$K = \frac{1}{3} Cpvl$$

Where *Cp* is the heat capacity of the material, *v* is the velocity of the phonons, and *l* is the mean phonon free path. Amorphous materials have a lower free path of phonons and low thermal conductivity compared to crystalline materials [44]. The influence of point defects on the free path of the phonons is described by equation 7.

Equation 7: scattering due to point defects.

$$l^{-1} = \frac{w^4 d}{4\pi v^3} \sum_i \Gamma_i$$

Equation 8: scattering cross-section of point defect.

$$\Gamma_i = x_i \left[\frac{(M - M_i)}{M}\right]^2 + \varepsilon \left[\left(\frac{\sqrt[3]{d} - \sqrt[3]{d_i}}{\sqrt[3]{d}}\right)\right]^2$$

Where *w* is the phonon frequency, *d* is the volume of the host atom, where x_i is the concentration of the defect, the mass of the host atom is *M* and the mass of the defect is M_i, ε is a phenomenological parameter and d_i is the volume of the defect[49].

In crystalline materials, phonon diffusion can be interrupted by phonon/phonon or phonon/defect scattering. Phonon/phonon scattering occurs when the atoms in the crystal lattice have anharmonic vibrations. Whereas, phonon/defect scattering occurs when a defect in the crystal interrupts the propagation of phonons [50][51][52][48].

An application for phonon/defect scattering is in materials dedicated to thermal barrier coatings (TBC). These materials are essential for high temperature operations. For example, materials with TBC are typically used in gas turbine engines. Studies of TBC materials have been developed during the last decades with two lines of research. The first one is to improve the low thermal conductivity of traditional materials such as $Ln_2Zr_2O_7$. The second one is the development of new materials with low thermal conductivity. In both cases, defects in the crystal lattice are the main mechanism influencing on thermal conductivity [33].

Another application for phonon/defect scattering was demonstrated by Yongguang Cheng et al. [6] in materials with NTE such as $In_{0.6}(HfMg)_{0.7}Mo_3O_{12}$. Oxygen vacancies alter the thermal properties of the material, enhanced the coefficient of NTE by about an order of magnitude larger, since polyhedra in the structure can increase flexibility due to oxygen defiency. Therefore, defects such as oxygen vacancies are for thermal conductivity in materials with NTE, such as of $Al_2W_3O_{12}$.

3
Objectives

3.1
General Objective

Analysis and characterization of point defects in $Al_2W_3O_{12}$ and their influence on thermal and optical properties.

3.2
Specific objetives

1. Production of different concentrations of oxygen vacancies through thermal excitation under reducing and inert atmospheres in $Al_2W_3O_{12}$.
2. Analyze the effect of temperatures and atmospheres on the formation and concentration of oxygen vacancies on $Al_2W_3O_{12}$.
3. Identification of the charge compensation mechanism in the $Al_2W_3O_{12}$ material.
4. Verification of the effect of oxygen vacancies on the coefficient of thermal expansion, thermal conductivity and optical properties in the UV-vis spectrum.

4
Materials and methods

4.1
Synthesis of $Al_2W_3O_{12}$ and oxygen vacancies generation

$Al_2W_3O_{12}$ was synthesized by co-precipitation. A white amorphous precipitate was obtained by mixture of $Al(NO_3)_3.9H_2O$ 0.1M (Alfa Aesar, purity ≥ 99%) with $Na_2WO_4.2H_2O$ 0.1M (Sigma Aldrich, St. Louis, MO, USA, purity ≥ 99%).

The white amorphous precipitate was centrifuged at 4000 rpm, during 6 min (NT 810, Novatecnica Piracicaba, Brazil) and washed three times with anhydrous ethanol (Vetec, 99.9%).

The amorphous $Al_2W_3O_{12}$ was dryied for three minutes in a conventional microwave oven. The $Al_2W_3O_{12}$ powder was heated in a horizontal tube furnace (Maitec-INTI FET 1600 / H, São Carlos, Brazil) for 10 hours at a temperature of 800 °C for crystallization. The crystallized powder of $Al_2W_3O_{12}$ is called Ar. This process described schematically in Figure 11.

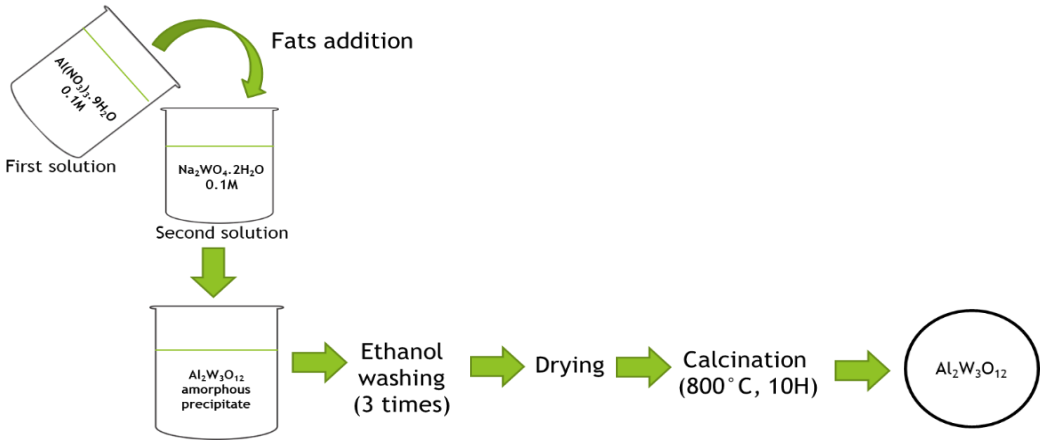

Figure 11: Schematic representation of the synthesis of $Al_2W_3O_{12}$ through co-precipitation by mixing reactants.

Ar sample was heat treated at 300, 400 and 500 °C under argon atmosphere. These samples were named as AAr300, AAr400, and AAr500. The Ar samples

were also heated in hydrogen atmosphere at 300, 400 and 500 °C. Samples were named as AH300, AH400, and AH500. These processes were carried out in a horizontal tube furnace (Maitec-INTI FET 1600 / H, São Carlos, Brazil).

4.2
Characterization of samples

4.2.1
X-ray power diffraction (XRPD) and high-temerature X-ray power diffraction (HT-XRPD)

The influence of oxygen vacancies on the crystal structure and CTE of the material was characterized by XRPD and high-temperature X-ray power diffraction (HT-XRPD) using D8 Advance diffractometer (Bruker, Germany) equipped with Anton-Paar XRK900 camera, using Cu Kα radiation. Room temperature diffractograms were obtained for all samples in a range from 10 ° to 80 ° (2 theta) with a step of 0.01 ° (2 s per step). The data obtained were analyzed using the Le Bail method with Topas 4.2 Software.

In situ diffractograms were obtained for samples AH400 and AAr400 at 25, 100, 150, 200, 250, 300, 350 and 400 ° C and in Ar samples 25, 100, 200, 250, 300 and 400 ° C.

4.2.2
Diffuse reflectance spectroscopy (DRS)

DRS was used to study the optical properties in all samples on a Perkin-Elmer Lambda 650 UV-vis spectrophotometer, in a range from 800 nm to 250 nm in 1 nm steps. The DRS data was used to estimate the value of the bandgap in all samples using the Kubelka-Munk function (equation 9).

Equation 9: Kubelka-Munk function

$$[F(R)hv] = A(hv - Eg)^n$$

Where *v* is the photons frequency, *h* is the Plancks constant, *Eg* is the bandgap energy and *A* is a constant. The exponent n is determined by the type of transition:

n= 2 for direct, allowed transition; n = 2/3 for direct, forbidden transition; n =1/2 for indirect transition allowed transition; n= 1/3 for indirect forbidden transitions [53][54].

With the data obtained from the Kubelka-Munk plots, it is possible to obtain more information about defects (i.e. oxygen vacancies) and relate them to the behavior of optical absorption. The absorption tail that appears in the Kubelka-munk plots after the energy of the bandgap is related to so-called Urbach energy (E_u) which is directly related to the number of defects states within the bandgap and to sub-bandgap transitions [55]. The Urbach energy is calculated using the reciprocal slope value of the linearized equation 10:

Equation 10: Equation to obtain the urbach energy

$$\alpha^* = \alpha_0 exp(hv - E_0/E_u)$$

Where α_0 and E_0 are the materials properties and α* is the absorption coefficient.

4.2.3 Electronic paramagnetic resonance (EPR) and Raman spectroscopy

The presence of oxygen vacancies in the samples was characterized by electronic paramagnetic resonance (EPR) and Raman spectroscopy. EPR were recorded on a commercial Miniscope 400 spectrometer (Magnettech-Germany) modified with a helium flow cryosystem, model ESR 900 (Oxford, England). For g factor calibration, a standard sample of ZnS: Mn with g = 2.0024 was used. The magnetic field is generated by a Varian electromagnet (9") powered by a current source from Heinzinger (Germany). EPR spectra were obtained at an optimized temperature of 300 K with magnetic field modulation at 100 kHz. Typical measurement parameters were microwave power 10 mW, scan time 60-300 s, central field 350 mT, and scan range 500 mT.

The Raman spectra were obtained through a microscope connected to a triple grating spectrometer (Jobin Yvon T64000 from Horiba), equiped with a CCD detector (charge coupled device) cooled by the Peltier effect. The samples were

excited by 532 nm laser line with 20mW power, and the spectrometer slots were set at a resolution of 2 cm^{-1}. Ramam spectra were taken using 2x40s in each spectral region.

4.2.4
X-ray excited photoelectron spectroscopy (XPS)

Characterization of the charge compensation mechanism was carried out with XPS. In the data collection, the Alpha 110 equipment was used with the VG thermo-hemispheric analyzer and Al Kα radiation (1486.6eV). The energetic correction was carried out with the metallic oxygen carbonates of the energy equal to 531.5 eV. The data obtained were analyzed with the casaXPS software.

4.2.5
Thermal conductivity test

The thermal conductivity of Ar, AH400 and AH400 was determined using the thermal transport option of a Quantum Design Physical Properties Measurement System (PPMS). A sample was prepared by pressing into a disk-shaped pellet with a diameter of 2.5 mm. A configuration of two probes attached to two disc-shaped copper wires was used. Thermal conductivity was measured under vacuum $1.3x10^{-2}$ Pa. The principles of operation for this technique are based on a pulse method and the measurement was taken in the steady-state mode.

5
Results and Discussion

5.1
Effect of oxygen vacancies on CTE

Figure 12(a-b) shows the comparison between the Ar sample and the samples calcined under hydrogen and argon atmospheres. The peaks of the diffractograms show the existence of a single orthorhombic $A_2W_3O_{12}$ phase regardless of the temperature or the atmosphere used in calcination.

(a)

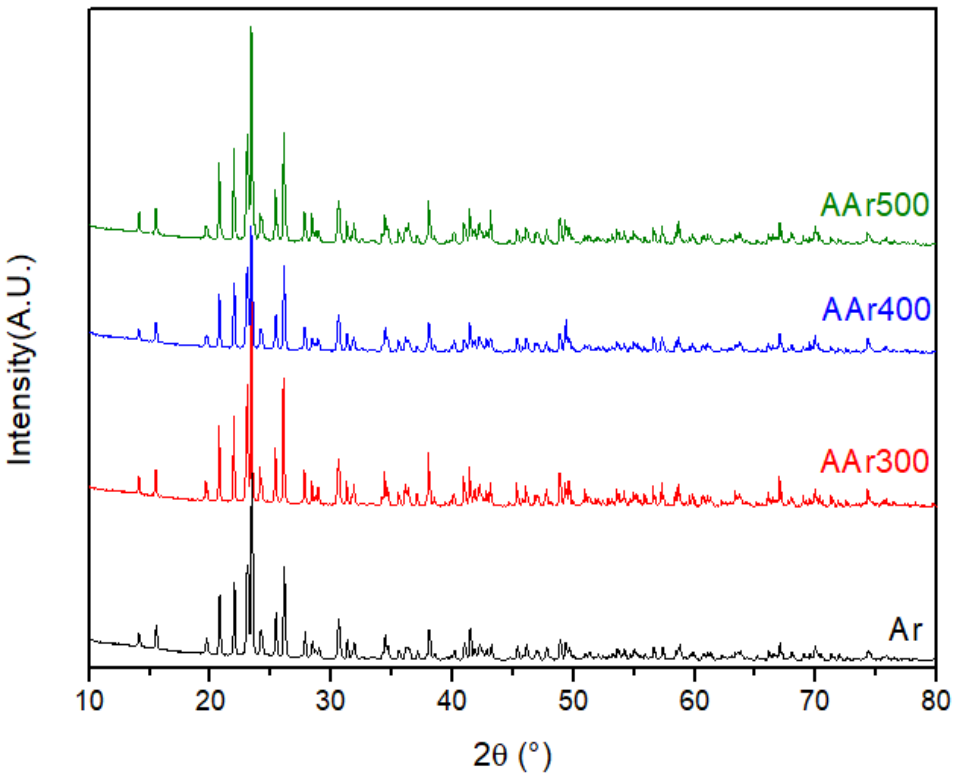

(b)

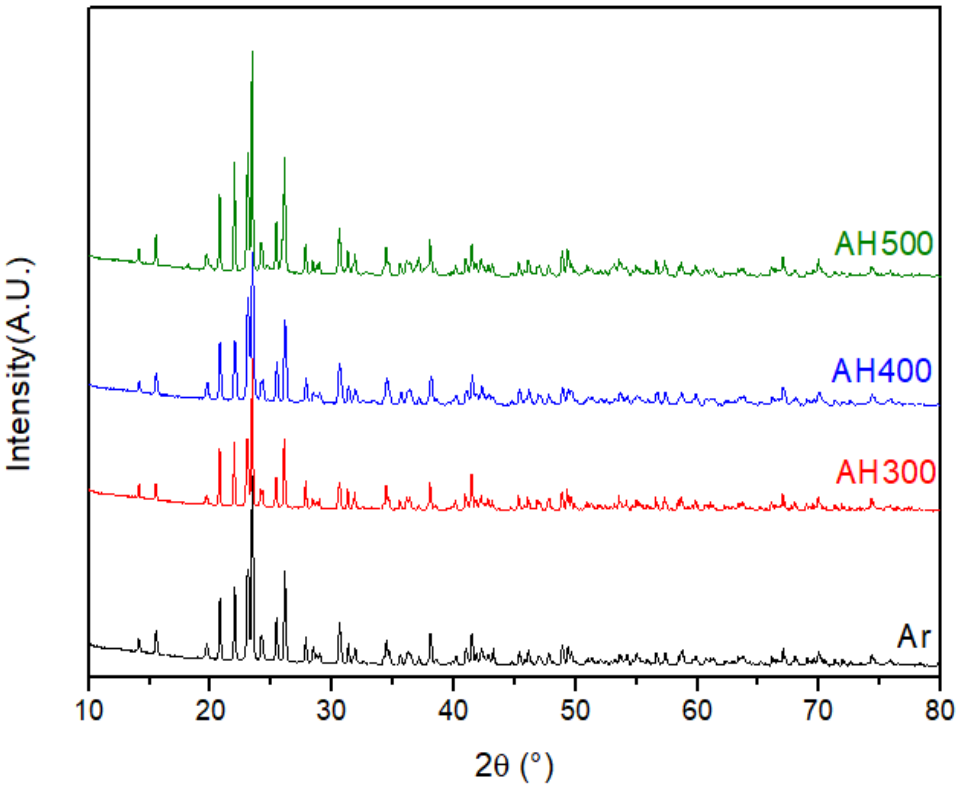

Figure 12: Comparison of XRD diffractograms of the (a) Ar, AH300, AH400 and AH500 and (b) Ar, AAr300, AAr400, and AAr500 samples.

Some researchers [46][56] observed a displacement of the diffraction lines to higher angles and suggested this may be due to the presence of oxygen vacancies. In Figure 12(a) and Figure 12(b), the shift of the diffraction lines is not easily visible. However, the unit cells for the samples Ar, AAr400 and AH400 are different, as shown in figure 14. Therefore in Figure 12(a) and Figure 12(b), there is a change in the diffraction lines despite not being visually identified.

In Figure 12 (a) and Figure 12 (b), the area under the diffraction lines at 14 and 15° was estimated using the OriginPro 2019b software, obtaining a baseline of 8 points with the 2nd derivative method. In the area under the first two peaks (i.e. 14 and 15 °), the values do not have a behavior that can be associated with the creation of oxygen vacancies (Appendix A for area under the first two peaks). The intensities of the diffraction lines situated at 14°, 15°, 20.7°, 21.9°, 23°, 23.4° have not presented a significant change as a function of atmosphere conditions. Therefore, the intensities of the peaks do not suggest the presence of oxygen vacancies in any of the samples, however, as Figure 14 demonstrates, there is an

influence on the orthorhombic phase of $Al_2W_3O_{12}$ due to the presence of oxygen vacancies.

On the other hand, orthorhombic phase is preserved at all temperatures for Ar, AH400 and AAr400 samples as shown in Figure 13(a-c). However, as shown in figure 14, oxygen vacancies increase unit-cell in the samples AH400 and AAr400 in comparison to the unit-cell of the sample treated only in the air. The influence on the unit-cell volumes have an influence on the CET, as shown in table 3.

(a)

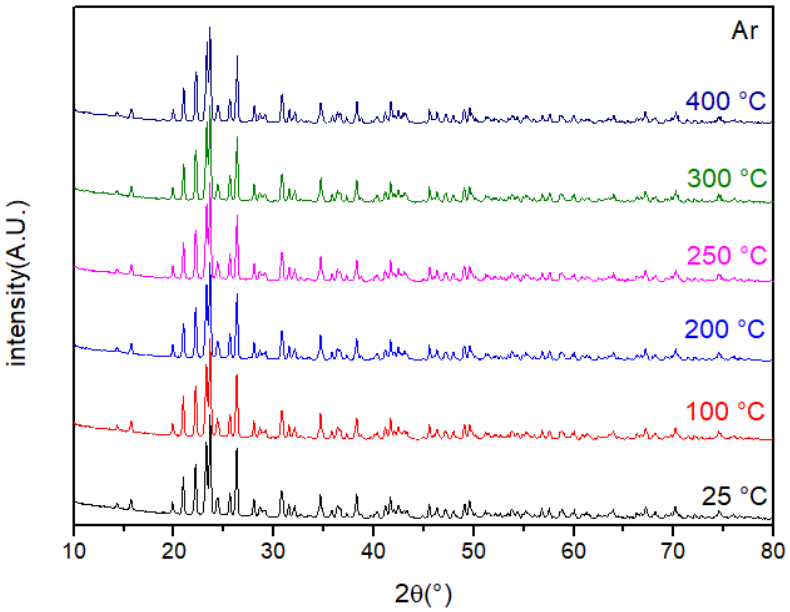

(b)

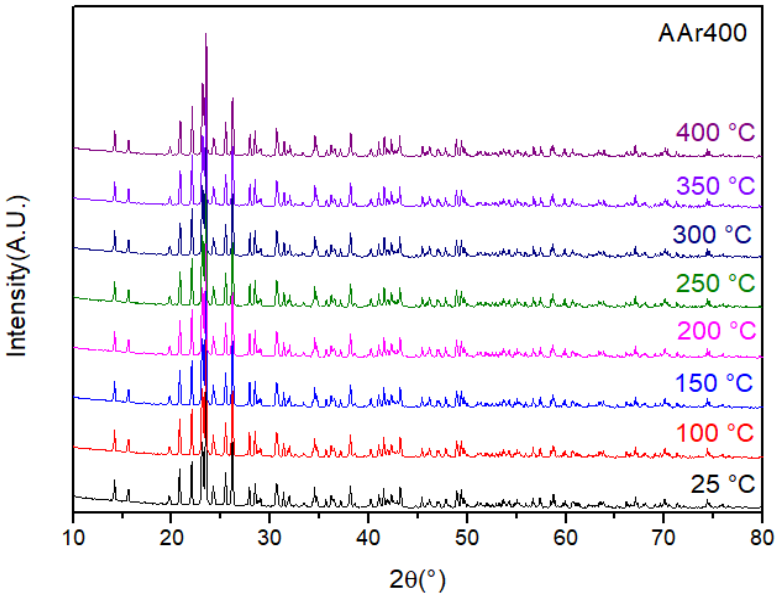

(c)

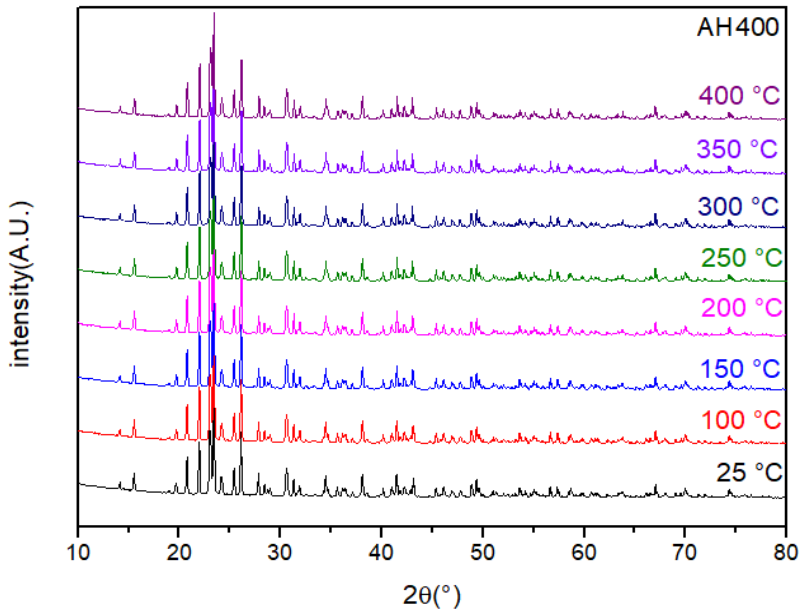

Figure 13: HT-XRD diffractograms of the (a) Ar, (b) AAr400 (c) and AH400 samples.

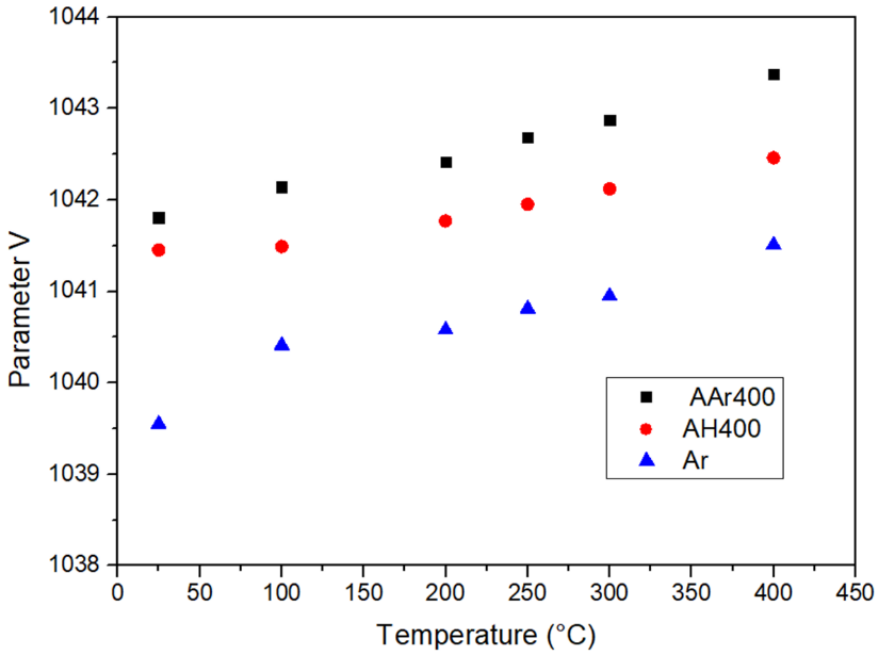

Figure 14 unit-cell volumes of the orthorhombic $Al_2W_3O_{12}$ in the AAR400 AH400 and Ar samples.

Table 3 presents the CTEs for the in the Ar, AH400, AAr400 samples, and for a previous study. The CTE values for the $Al_2W_3O_{12}$ in the Ar sample are reasonably close to those previously reported in Chapter 2 (Table 1). Interestingly, the CTE in the $Al_2W_3O_{12}$ decreases with the increase of oxygen vacancies. Oxygen vacancies may caused crystal framework more flexible and this additional flexibility may facilitate transverse vibrations, which contribute to the NTE properties of the material. This decrease in CTE with the addition of oxygen vacancies is consistent with the findings reported in some previous studies [6][57][58][59].

Table 3: CTE (α) for orthorhombic $Al_2W_3O_{12}$ in different samples, obtained using HT-XRPD. α_l Represents the Averaged Linear Thermal Expansion Coefficient, and α_v, volumetric CTE.

Ref.	Sample	α_a ($10^{-6}K^{-1}$)	α_b ($10^{-6}K^{-1}$)	α_c ($10^{-6}K^{-1}$)	α_l ($10^{-6}K^{-1}$)	α_v ($10^{-6}K^{-1}$)
[11]	$Al_2W_3O_{12}$	5.94	-0.099	-1.31	1.5	4.51
This work	Ar	6.5796	-0.6473	-1.4097	1.5075	4.4578
This work	AAr400	5.902	-0.7084	-1.4222	1.2571	3.7713
This work	AH400	5.4074	-1.019	-1.68	0.9026	2.7414

5.2
Effect of oxygen vacancies on optical properties

Powders synthesized by the co-precipitation method with the addinitonal introduction of oxygen vacancies by thermal treatment in argon or hydrogen atmospheres showed different colors related to the adopted heat thermal treatment. The differently heat-treated samples are shown in Figure 15.

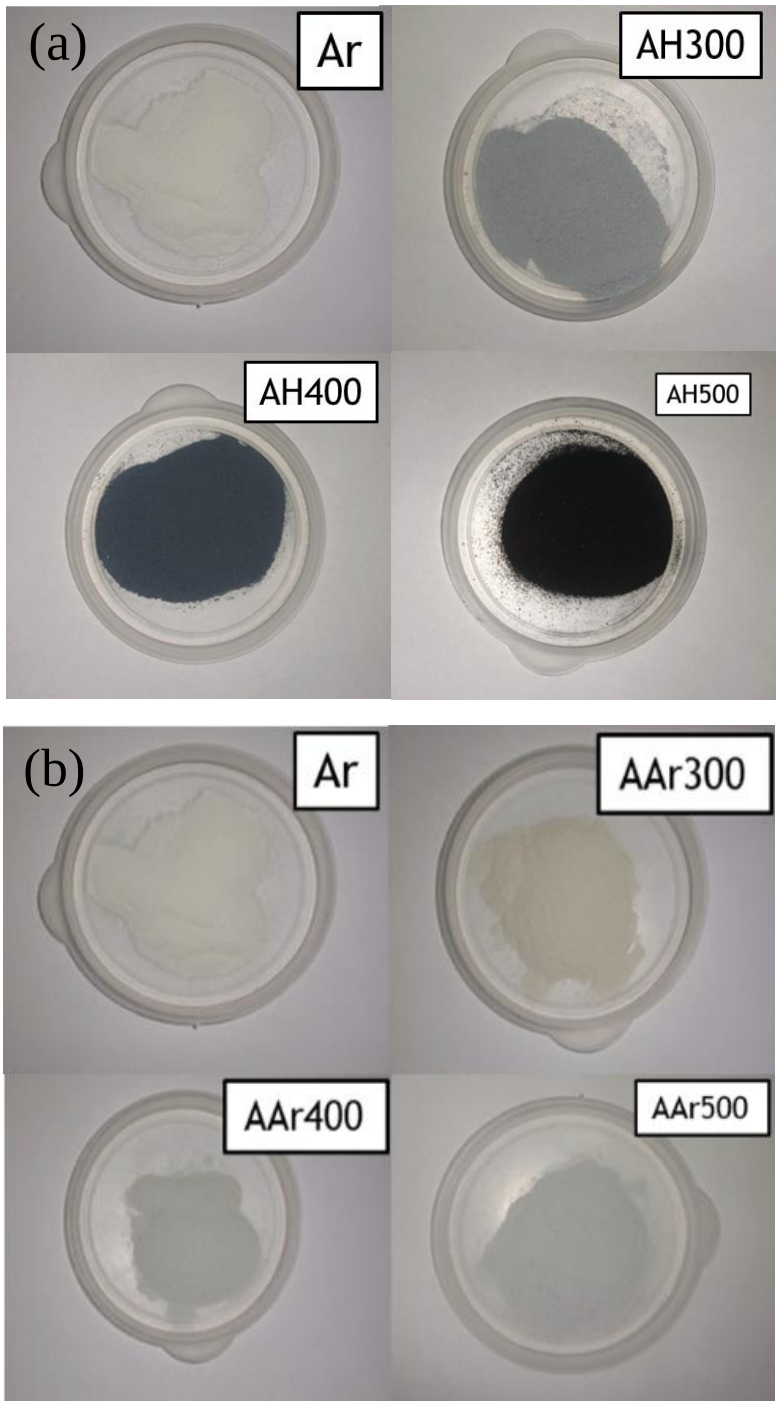

Figure 15: Samples treated within (a) hydrogen atmosphere (AH300, AH400, and AH500) and Ar sample, for comparison, and (b) argon atmosphere (AAr300, AAr400 and AAr500) and Ar sample, for comparison.

Figure 15 shows monophasic $Al_2W_3O_{12}$ powders with a color changing from white to black. The color change indicates sensitization in the visible spectrum, probably caused by the formation of oxygen vacancies, indirectly confirmed by

DRS analysis that indicates an increased absorption of the visible spectrum, as evidenced in Figure 16.

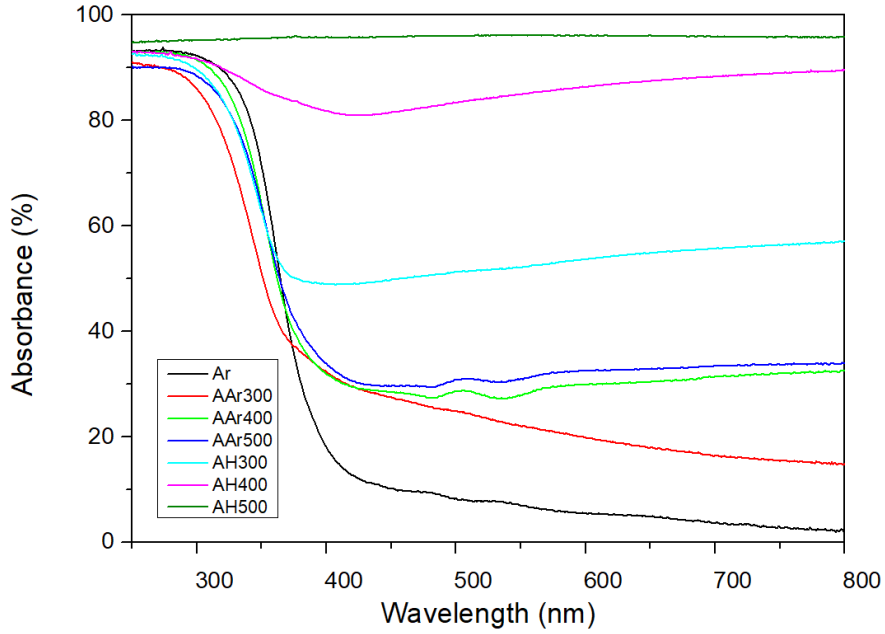

Figure 16: DRS curves for Ar, AH300, AH400, AH500, AAr300, AAr400 and AAr500 samples.

According to DRS results (Figure 16), the Ar sample only shows significant absorption in the UV spectral region (250-400 nm) and low absorption in visible part of spectrum. On the other hand, the samples treated with hydrogen and argon atmospheres showed strong absorption in the visible spectra.

The DRS curve of AH400 and AH500 showed the highest absorbance throughout the visible spectrum, among all samples. For the AH300 sample, the percentage of absorbance remains constant between 400 and 800 nm in ~50 %. Samples treated with hydrogen atmosphere showed strong absorption of the UV-vis spectra, which is in accordance with some other studies [60].

In the samples treated with argon atmosphere, absorbance in the visible spectrum region is lower than in hydrogen treated samples, which explains beige color in the AAr300, AAr400 and AAr500 samples.

In respect to the calcination temperature, the samples treated at higher temperatures presented a high percentage of absorbance.

The Kubelka-Munk function was used to calculate the value of the band-gap in all samples (Figure 17 a and b) considering the indirect transition (n = 1/2), as previously reported for $Al_2W_3O_{12}$ [15][20].

(a)

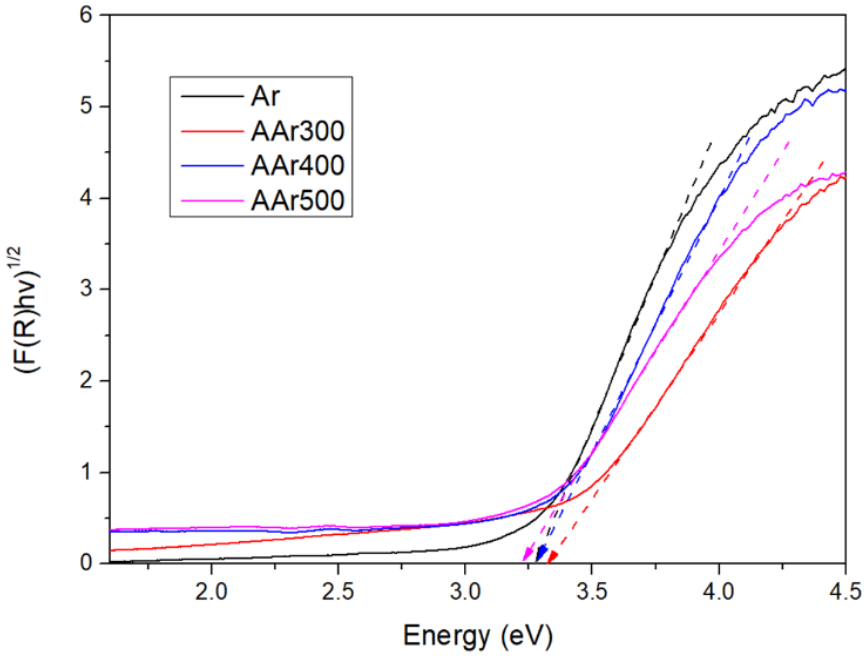

(b)

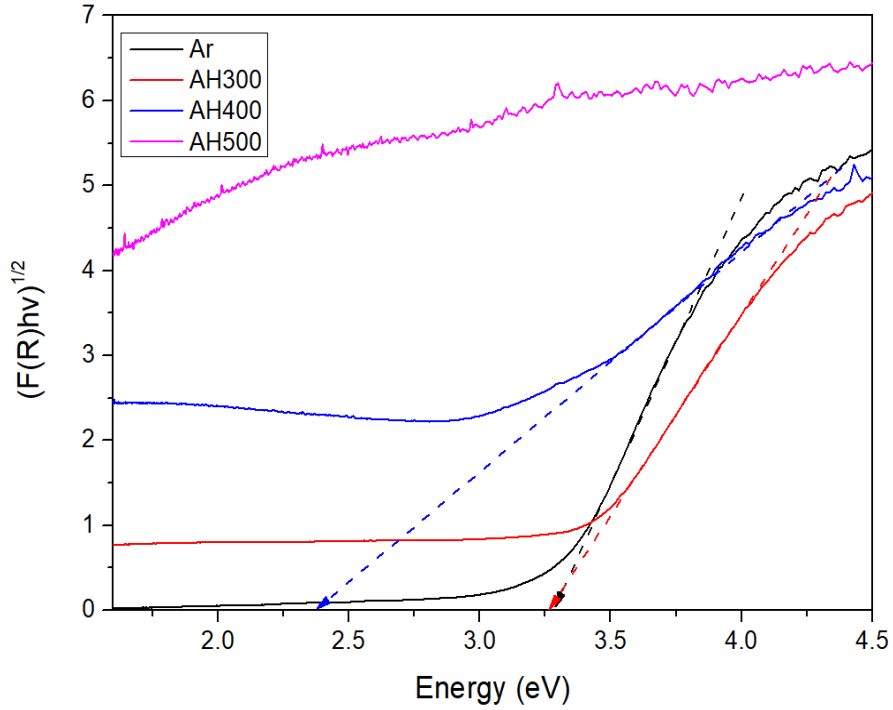

Figure 17: Kubelka-Munk plot for the sample (a) Ar and argon atmosphere treted samples (AAr300, AAr400 and AAr500) and (b) Ar and hydrogen atmosphere treated samples (AH300, AH400 and AH500).

Band-gap values between 3.11 and 3.4 eV were reported in $Al_2W_3O_{12}$, free of oxygen vacancies [15][20]. The sample Ar presents a band-gap value of 3.26 eV, in accordance with the reported values. This difference between the reported values is possibly due to the fact that band-gap in nanoparticulate materials can be affected by lattice strain in the sample and surface and interface effect [61].

The value of the bangap decreased when the temperature is increased. In AH300 (Eg= 3.24 eV) and AH400 (Eg= 2.29 eV) the value of the bandgap decreased considerably, indicating the presence of intermediate levels in the bandgap. However, in the sample AH500 it was not possible to calculate the band gap value at all, due to the high absorption in the whole visible light spectrum. The AAr300 (Eg= 3.35eV), AAr400 (Eg= 3.26 eV) and AAr500 (Eg= 3.21 eV) samples showed a small decrease in the value of the bandgap with the increase of temperature. The decrease in the value of the forbidden band for all calcined samples indicates that high temperatures promoted a higer concentration of oxygen vacancies.

On the other hand, Figure 18 shows the energy contribution of the oxygen vacancies within the bandgap obtained with the procedure reported in chapter 4.2.2.

(a)

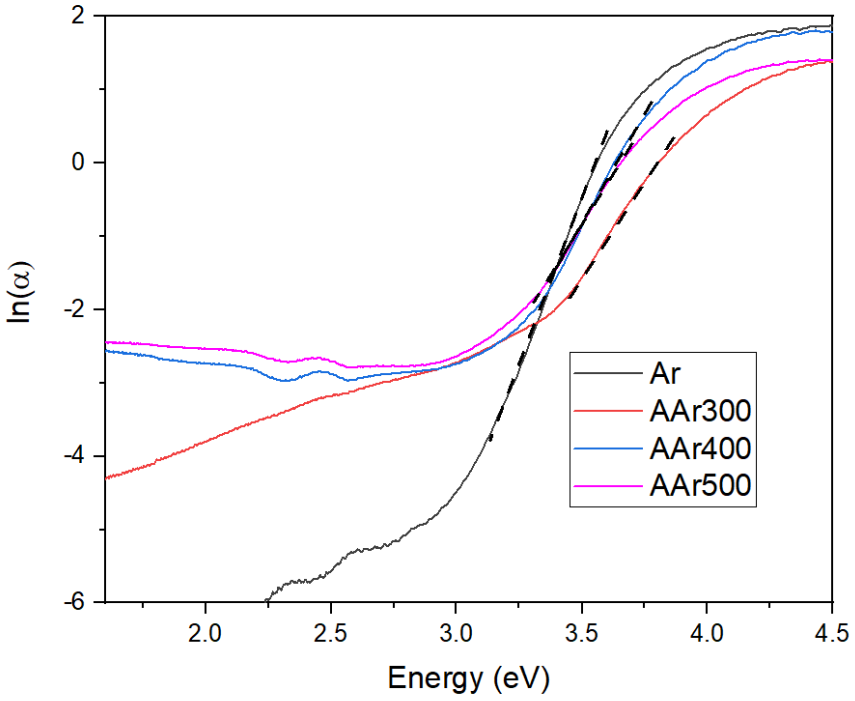

(b)

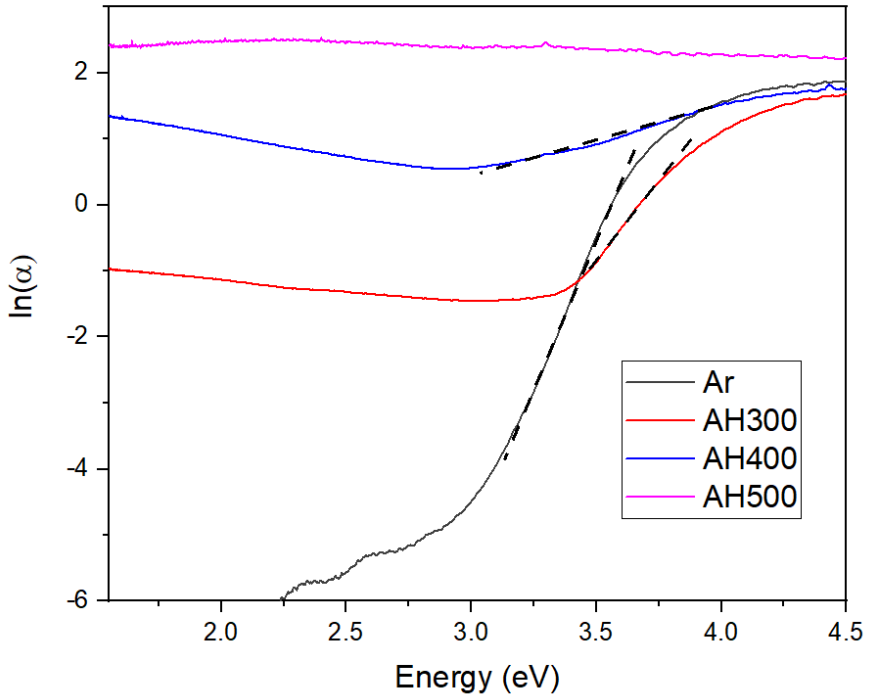

Figure 18 Urbach energy graphs obtained from Kubelka-Munk plots of (a) Ar and the samples treated in argon atmosphere (AAr300, AAr400 and AAr500) and (b) Ar and the samples treated in hydrogen atmosphere (AH300, AH400 and AH500).

Figure 18 shows the change in slopes that can be an indirect sign of the change in oxygen vacancy concentration. This indicates a formation of new oxygen vacancies, which is reinforced by the results of the DRS (Figure 16) and the change in E_g (Figure 17).

The behavior of the AH500 sample observed in figure 18 (b) makes it difficult to read the Urbach energy, since the sample shows a slight negative slope and this suggests an atypical contribution of the oxygen vacancies to the sample, which is physically improbable. For this reason, it was not possible to calculate the Urbach energy in this sample. Finally, the other evaluated samples showed a reasonable behavior, in accordance with other studies [62][63][64].

Table 4 shows the Urbach and bandgap energies for all samples. It is possible to establish a direct relationship between the Urbach energy and the energy of the bandgap. The Urbach energy is inversely proportional to the energy of the bandgap. The behavior of the Urbach energy shows the influence of oxygen

vacancies on the bandgap, suggesting that the creation of new oxygen vacancies within the crystal lattice of $Al_2W_3O_{12}$ decreases the bandgap. In other words, the concentration of oxygen vacancies should increase with the severity of thermal treatment, being the most severe conditions with the highest concentration of oxygen vacancies, the hydrogen treatment at 500 ºC. Please, consult Appendix B for Urbach energy calculation.

Table 4: Urbach and band gap energies for all samples.

Samples	Eg (eV)	E_u(meV)
Ar	3.26	116.82
AAr300	3.35	201.84
AAr400	3.26	161.17
AAr500	3.21	180.94
AH300	3.24	225.22
AH400	2.29	856.93
AH500	--	--

5.3
Study of oxygen vacancies

Raman spectroscopy was used, at room temperature, to identify the presence of oxygen vacancies. The vibratory modes inside $Al_2W_3O_{12}$ are classified into four regions. Peaks ν_1 in the range of 100-300 cm^{-1} belong to lattice vibrations of WO_4, ν_2 in the range of 300-500 cm^{-1} to bending vibrations of O-W-O in WO_4, ν_3 in the range of 700-900 cm^{-1} to the asymmetric stretching vibration of W-O in WO_4 and ν_4 in the range of 950-1050 cm^{-1} to the symmetric stretching vibration of W-O in WO_4 [25] [22] [65][66].

Figure 19 shows the Raman spectrum of AAr300, AAr400, AAr500, and Ar samples. The four spectra show the vibrational modes ν_1, ν_2, ν_3 and ν_4. The spectra showed the same Raman signals in all spectral regions without apparent

displacement of bands. Therefore, it was not possible to identify the presence of oxygen vacancies by Raman spectroscopy in the samples treated with argon.

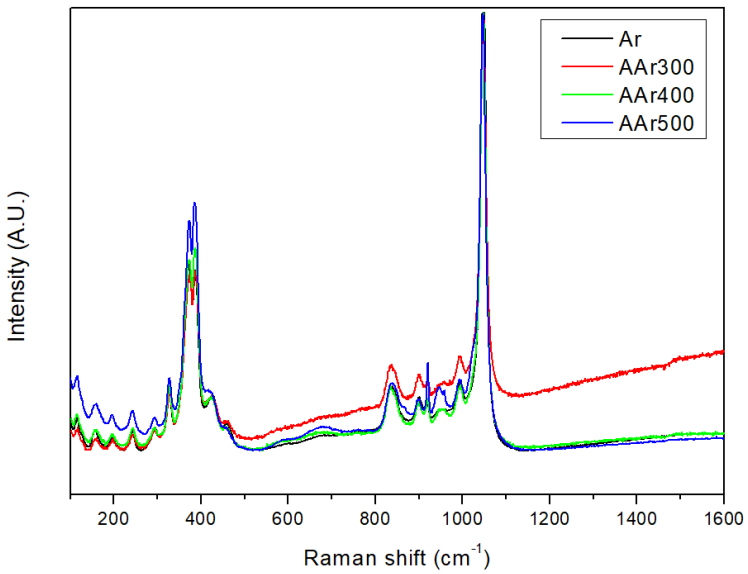

Figure 19: Raman spectra of the AAR300, AAR400 AAR500 and Ar samples in 150-1600 cm^{-1} region.

Spectra normalized to samples treated with hydrogen atmosphere can be seen in Figure 20. The Raman spectrum shows the signals corresponding to the modes of the vibrational modes ν_1, ν_2, ν_3 and ν_4. Since there were no additional signals, the samples are homogeneous and without impurities.

(a)

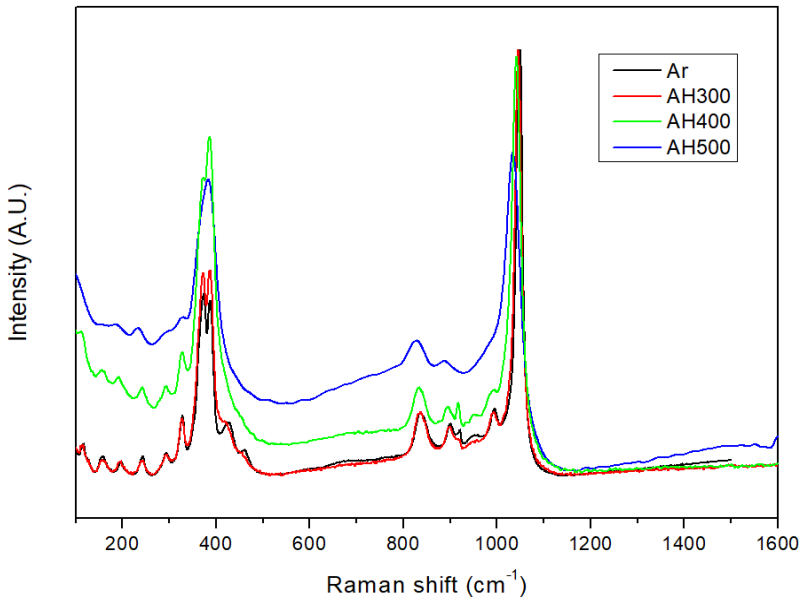

(b)

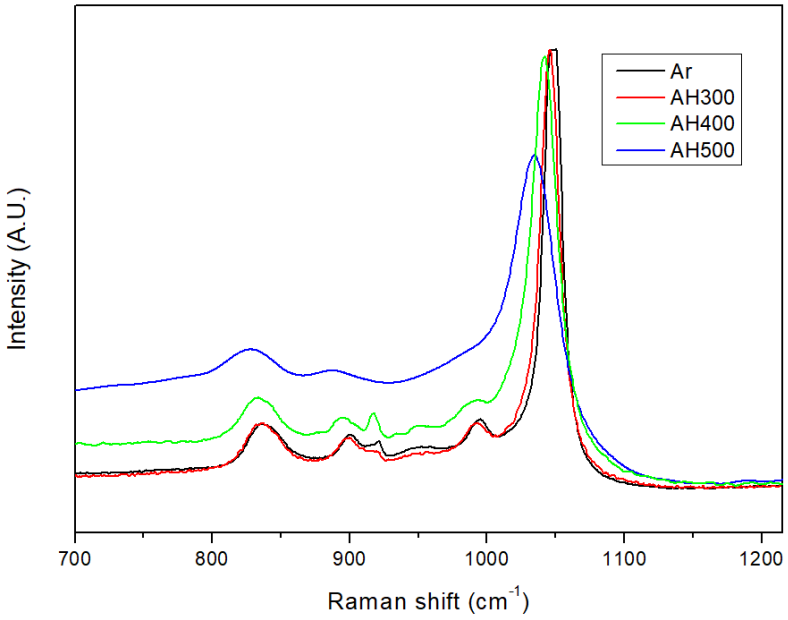

Figure 20: Raman spectra of the AH300, AH400 AH500 and Ar samples in (a) 150-1600 cm^{-1} and (b) 700-1220 cm^{-1}.

It was observed that with the increase in calcination temperature, the Raman signal became weaker. This is due to the presence of point defects, such as oxygen vacancies, in the crystal lattice. This was also confirmed by the shift towards a lower wavenumber in the ν_4 and ν_3 regions, also known as red-shift.

Figure 20 shows a red-shift for ν_3 and ν_4, which might be an indication of presence of oxygen vacancies [60]. The partial absence of oxygen in the crystal lattice indicates a change of the crystal field and the structure relaxation.

Table 5 shows the location of the Raman signals, and it is possible to observe the displacement of the signals. For example, in the signals of the ν_4 region, the signal at 1048 cm^{-1} for the sample Ar shows a displacement toward lower wavenumbers for the samples AH300 (1045 cm^{-1}), AH400 (1041cm^{-1}) and AH500 (1034 cm^{-1}). The displacement behavior is observed for the other signals, such as in the region of asymmetric stretching for AH300 (835 cm^{-1}), AH400 (833 cm^{-1}) and AH500 (828 cm^{-1}).

Table 5: Raman signals of Ar, AH300, AH400 and AH500 samples for asymmetric stretching and symmetric stretching.

Samples	Asymmetric stretching vibration of W–O in WO_4	Symmetric stretching vibration of W–O in WO_4
Ar	837-900-920-949 cm^{-1}	994-1048 cm^{-1}
AH300	835-895-919 cm^{-1}	990-1045 cm^{-1}
AH400	833-893-916 cm^{-1}	1041 cm^{-1}
AH500	828-886 cm^{-1}	1034 cm^{-1}

On the other hand, in the samples with higher absorption of the UV-vis spectrum (i.e. AH300, AH400 and AH500 samples) weaker Raman signals are obtained because the defects in the crystalline structure caused an alteration in the intensity of the peaks of the Raman spectroscopy, which agrees with some other studies [65][66][60][67]. Therefore, it is possible to establish a relationship between the Raman spectroscopy and DRS data. High absorption of the UV-vis spectrum makes it more difficult to read the signals of the Raman spectrum. This suggests that the optical properties of $Al_2W_3O_{12}$ are affected by the presence of oxygen vacancies.

By EPR more information was obtained about the presence of oxygen vacancies in the samples since with this technique it is possible to identify directly identify their existence [68]. A comparison was made in the EPR signals for the Ar sample with the other samples (Figure 21) and a strong signal was observed at g = 2.00 for the samples AH500 AH400 and AAr300. This signal can be attributed to a single electron trapped oxygen vacancy (SETOV) according to other studies [69][70][71].

The increase in the intensity of the signal may be attributed to a higher concentration of oxygen vacancies [72]. The signal at g = 2.00 increases as a function of the calcination temperature and it is the highest for the sample AH500. In the samples Ar and AAr500, the signal at g = 2.00 is too weak to be attributed to the presence of oxygen vacancies. On the other hand, samples AAr400, AAr300, and AH300 show a weak signal that may be an indication of the presence of oxygen vacancies.

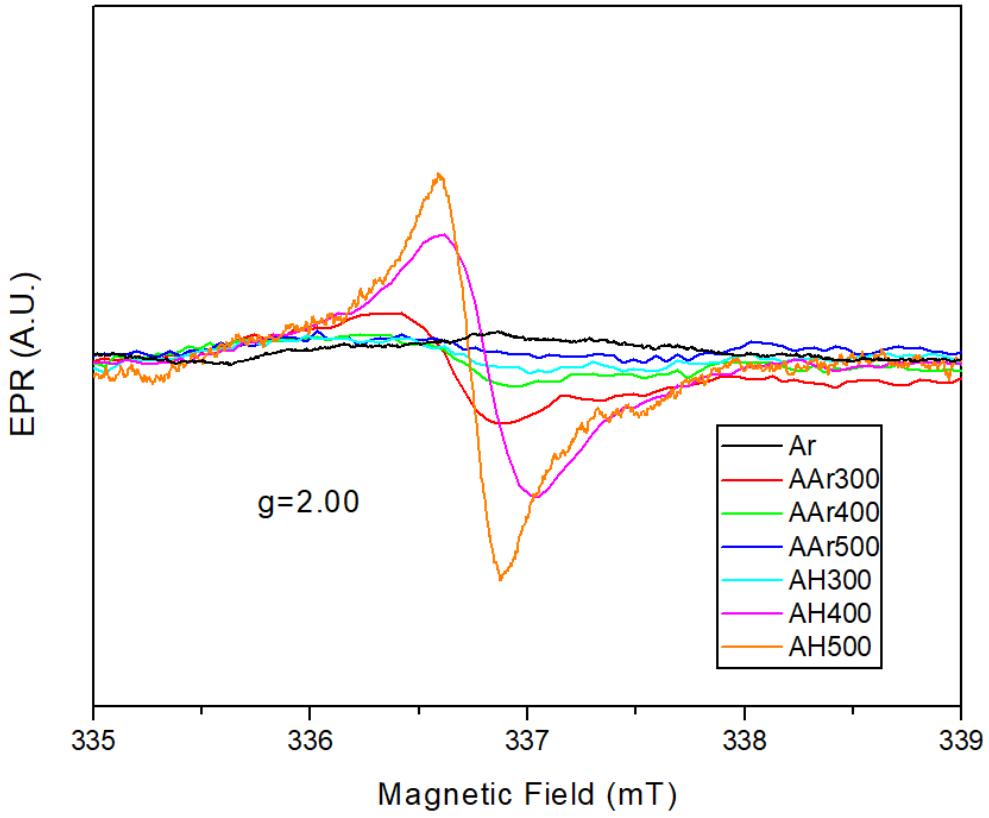

Figure 21: EPR spectra of the samples Ar, AAr300, AAr400, AAr500 AH300 AH400 and AH500.

The data obtained from the EPR and the Raman spectroscopy confirmed the results obtained for AH500 and AH400 with the DRS (Figure 16). These results suggest the presence of high concentrations of oxygen vacancies in thermal treatments of 400 and 500 C° and for hydrogen atmospher. On the other hand, for the samples treated with argon atmospheres at different temperatures, the concentration of oxygen vacancies is lower.

5.4
Determination of valence states of point defects

The XPS spectrum for the sample denoted Ar (figure 22) shows the presence of W^{6+} at 36.09 eV assigned to W $4f_{7/2}$ and 38.29 eV assigned to W $4f_{5/2}$. In addition, two smaller peaks are also observed at 34.9 eV and 37.1 eV, corresponding to W $4f_{7/2}$ and W $4f_{5/2}$, assigned to W^{5+}.

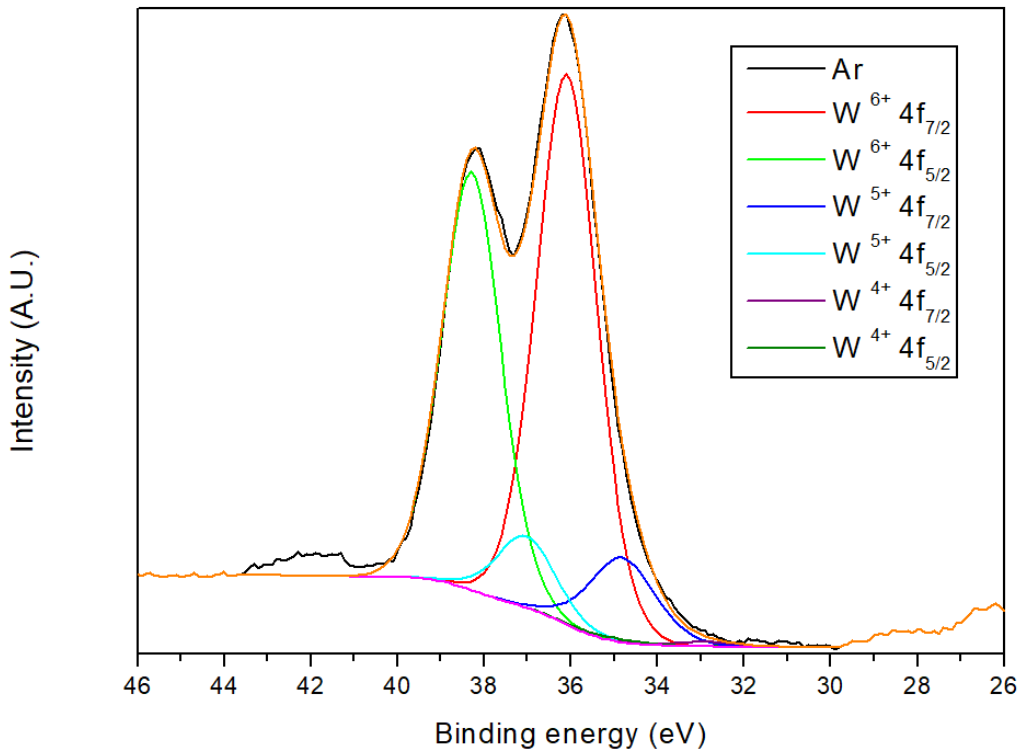

Figure 22: XPS spectra of sample Ar.

The XPS spectra of the samples treated within the argon atmosphere are presented in Figure 23 (a-c). Samples AAr300, AAr400, and AAr500 show the presence of a new valence state for W (W^{4+}). In Figure 23 a, corresponding to the AAr300 sample, the presence of W^{4+} can be identified thorugh the bands at 32.94 eV for W$4f_{7/2}$ and 35.34 eV for W$4f_{5/2}$. In the AAr400 sample (Figure 23 b), the signals corresponding to W^{4+} are observed at 32.90 eV for W$4f_{7/2}$ and 35.10 eV for W$4f_{5/2}$. In AAr500 sample (Figure 23 c), the W^{4+} signal is identified for W$4f_{7/2}$ at 32.92 eV and W$4f_{5/2}$ at 35.32 eV. In both samples the presence of states W^{6+} and W^{5+} is observed. This indicates that due to the formation of oxygen vacancies the W modifies the valence state from W^{6+} to W^{5+} and to W^{4+} and thus keeping the charge stability in $Al_2W_3O_{12}$.

(a)

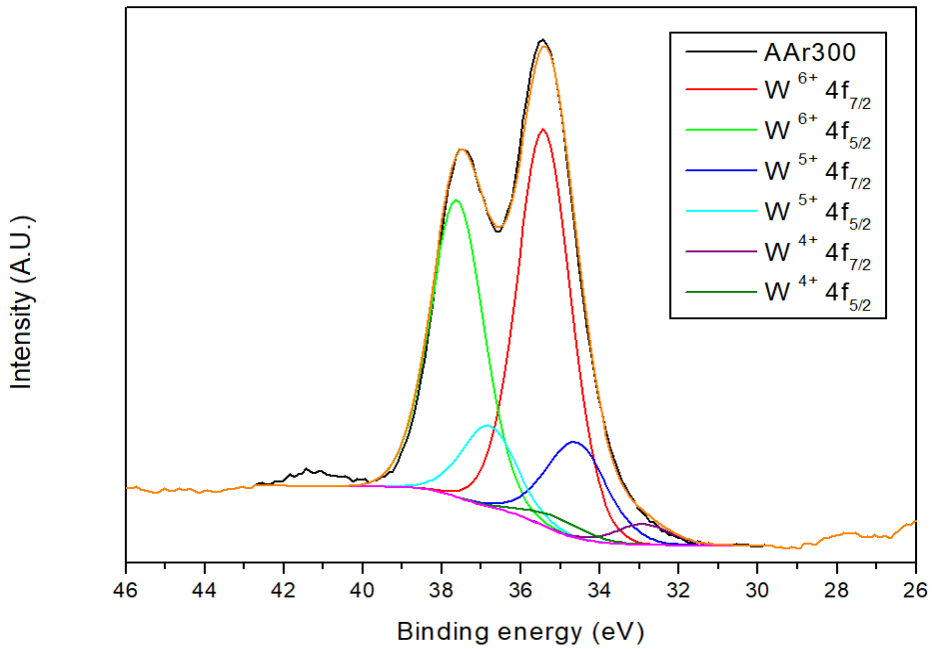

(b)

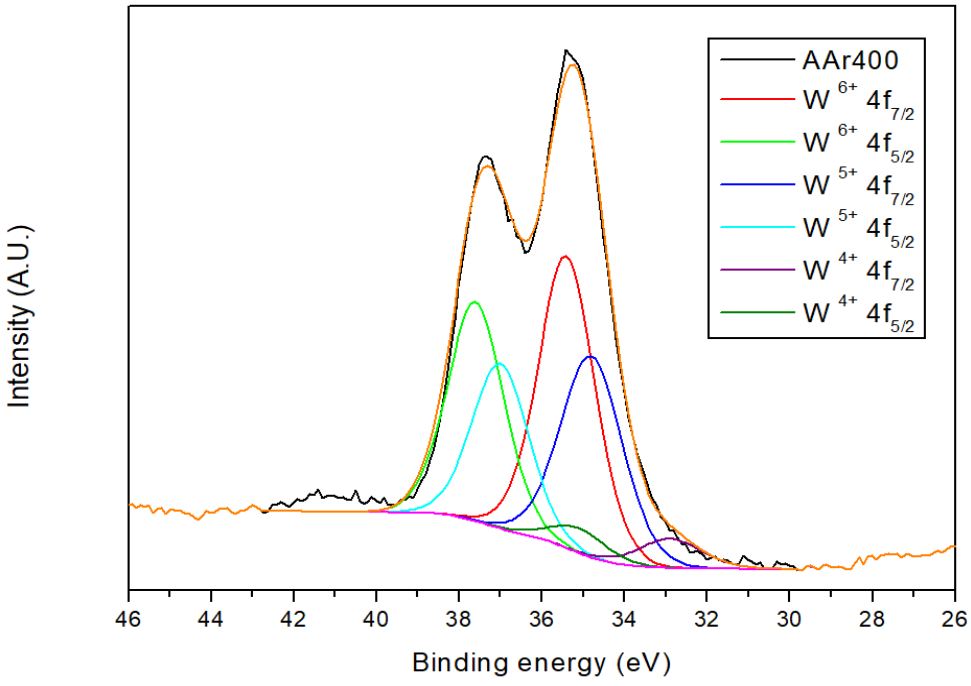

(c)

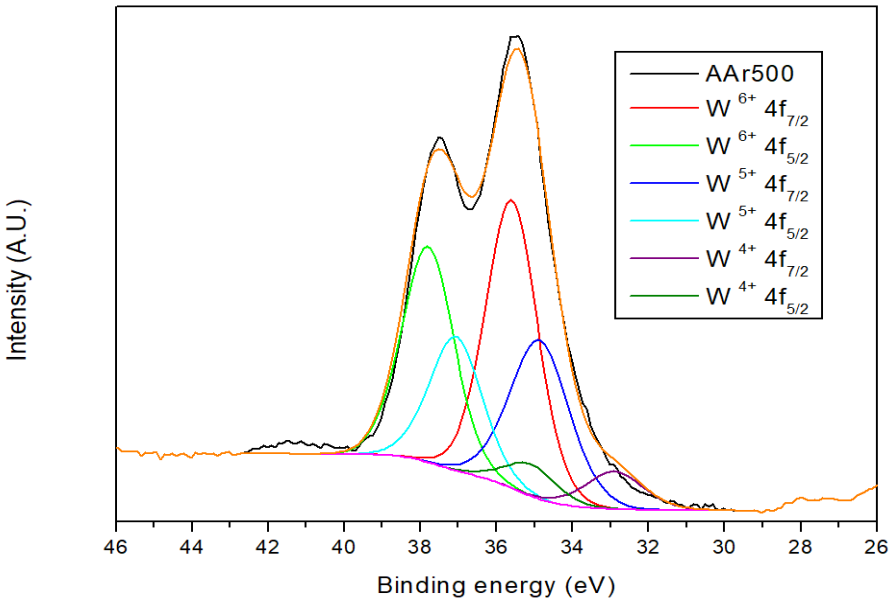

Figure 23: XPS spectra for samples AAr 300(a), AAr400(b) and AAr500(c).

Table 6 shows the percentage of W cations with different valencies, as estimated from the areas below corresponding peaks, in the samples treated with argon atmosphere and in the sample denoted Ar. According to the estimated percentage, it is possible to observe a decrease in W^{6+} content with the increase in temperature and the increase in W^{5+} and W^{4+} valences in the samples with thermal treatments at higher temperatures. Based on the values of the AAr400 and AAr500 samples it can be understood that in inert atmospheres and at thermal treatments of 400°C or higher, the concentration of oxygen vacancies is almost constant.

Table 6: The content of W^{6+}, W^{5+} and W^{4+} species in the samples Ar, AAr300, AAr400 and AAr500 based on the area of peaks at XPS spectra, of each cationic species.

Samples	W^{6+} (%)	W^{5+} (%)	W^{4+} (%)
Ar	84.83	14.47	0.7
AAr300	75.41	20.04	4.04
AAr400	53.6	40.36	6.04
AAr500	56.05	35.64	8.3

XPS spectra of the sample AH300, AH400 and AH500 are presented in Figure 24(a-c).

(a)

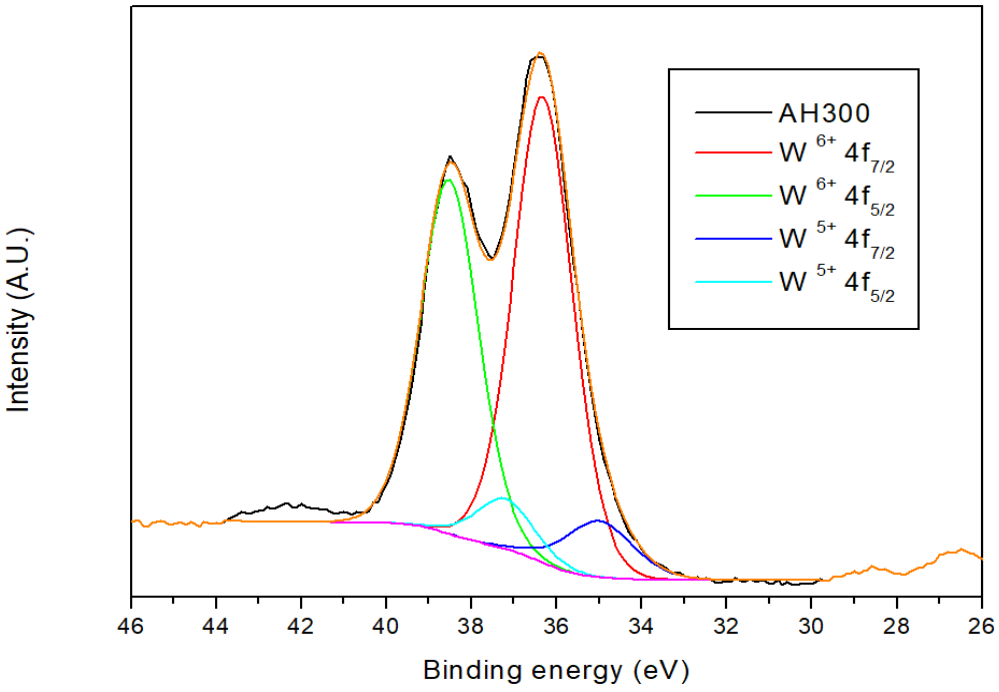

(b)

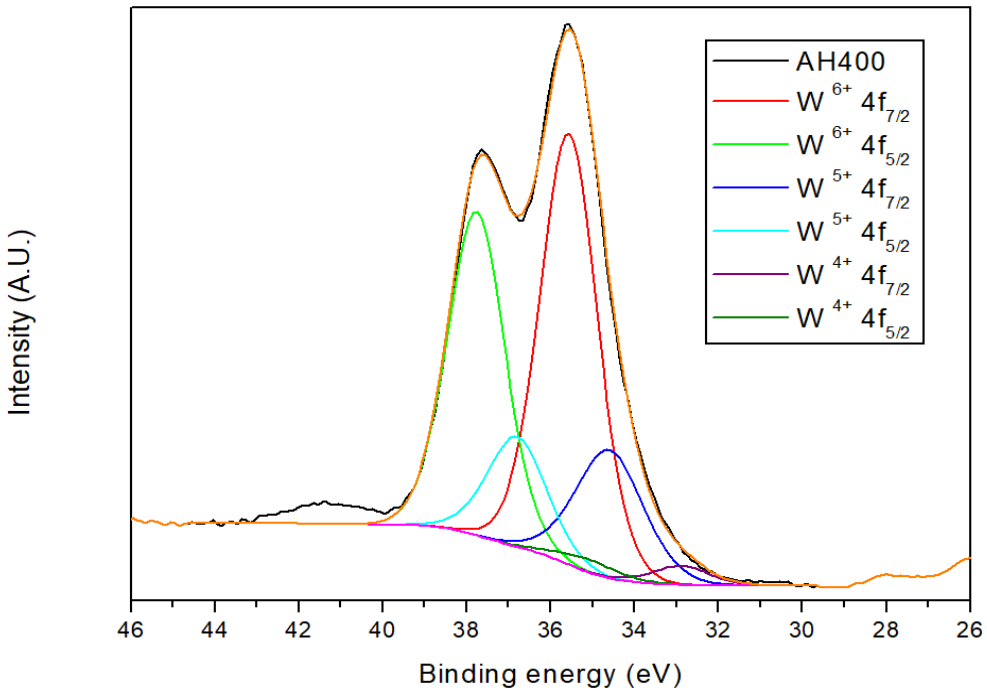

(c)

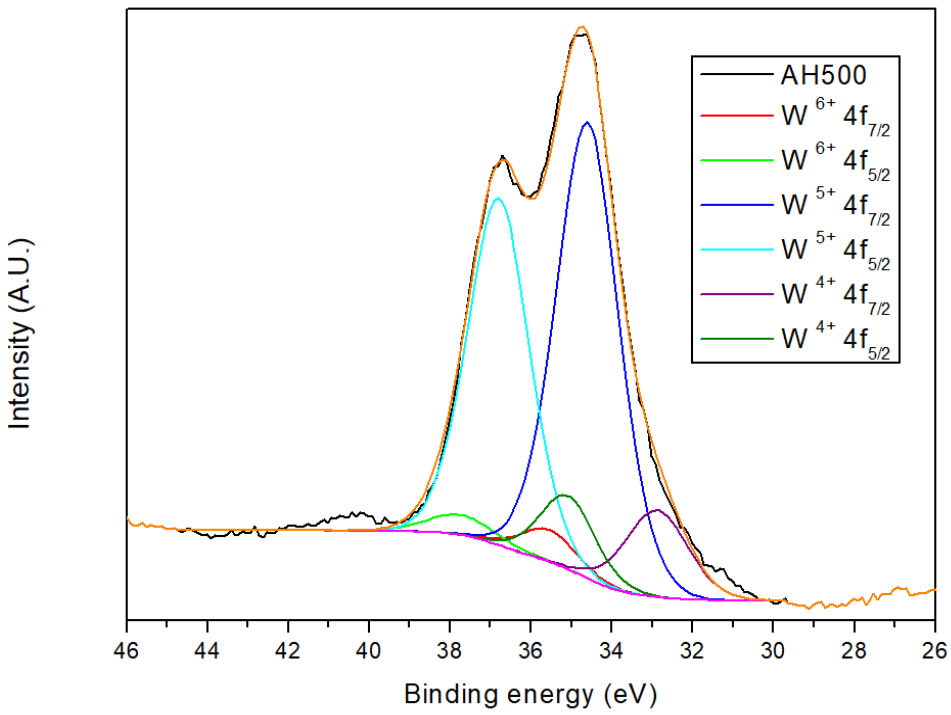

Figure 24: XPS spectra for samples AH300(a), AH400(b) and AH500(c).

In the AH300 sample only shows the presence of 4 peaks. In Figure 24a, corresponding to sample AH300, the signals at 36.3 eV and 38.5 eV correspond to $W4f_{7/2}$ and $W4f_{5/2}$ are values assigned for W^{6+}, and the state W^{5+} is assigned for the signals at 35 eV for $W4f_{7/2}$ and at 37.3 eV for $W4f_{5/2}$.

In samples AH400 and AH500 the presence of W^{4+} can be observed, reperented by the peaks at 32.9 eV and 35.22 eV for $W4f_{7/2}$ and $W4f_{5/2}$, respectively. The presence of W^{5+} is also observed in the two samples, at 34.5 eV for $W4f_{7/2}$ and 36.82 eV for $W4f_{5/2}$. The increase in W^{5+} or W^{4+} and the decrease in W^{6+} in samples AH400 and AH500 is observed.

The Table 7 shows the percentages of W with W^{4+}, W^{5} and W^{6+}, as estimated from the areas below corresponding peaks into samples treated with hydrogen atmosphere and the sample Ar. The presence of only two valences for W (W^{6+} and W^{5+}) in AH300 sample shows that it is necessary to use higher temperatures in a hydrogen atmosphere to produce W^{4+}.

Table 7: The content of W^{6+}, W^{5+} and W^{4+} species in the samples Ar, AH300, AH400 and AH500 based on the area of peaks at XPS spectra, of each cationic species.

Samples	W^{6+} %	W^{5+} %	W^{4+} %
Ar	84.83	14.47	0.7
AH300	87.73	12.27	--
AH400	71.29	25.55	3.17
AH500	4.88	80.03	15.09

The existence of oxygen vacancies can modify the valence states of W from W^{6+} to W^{5+} or even to W^{4+}, as reported by this and some other studies [69][35][60]. The presence of W^{6+}, W^{5+} or W^{4+} is possible since the WO_3 and WO_2 phases can coexist in the system [72], together with $Al_2W_3O_{12}$ with oxygen vacancies and reduced W species such as W^{5+} and W^{4+}. This later is a consequence of the charge compensation necessary for charge stability caused by the presence of the oxygen vacancy.

One electron localized in oxygen vacancies (*i.e.* $Vo^{\bullet}$) modifies the valence W^{6+} to W^{5+}, as proved by the SETOV signal from the EPR. However, the XPS of the samples showing the presence of W^{4+}, suggested that two electrons localized in an oxygen vacancy site (i.e. $Vo^{\bullet\bullet}$) were also present in the samples. Therefore, it is necessary to consider the existence of $Vo^{\bullet}$ and $Vo^{\bullet\bullet}$ in the $Al_2W_3O_{12}$ material. The presence of oxygen vacancies generates sublevels within the bandgap and produces new color centers [34], in agreement with the color change in the samples and in accordance with the results obtained from the DRS.

On the other hand, Equations 11 and 12 represent the valence change of W^{6+} to W^{4+} or W^{5+} in $Al_2W_3O_{12}$ under argon and hydrogen atmospheres.

Equation 11: Kröger-Vink notation for $Al_2W_3O_{12}$ under argon and hydrogen atmospheres where W^{6+} to W^{4+}.

$$W_W^x \rightarrow W_W^{''} + V_o^{\bullet\bullet}$$

Equation 12: Kröger-Vink notation for $Al_2W_3O_{12}$ under argon and hydrogen atmospheres where W^{6+} to W^{5+} under argon and hydrogen atmospheres.

$$W_W^x \rightarrow W_W^{'} + V_o^{\bullet}$$

It is possible to establish tentatively a 1:1 relationship between W and the generation of oxygen vacancies. This means that for each W^{4+} a $Vo^{\bullet\bullet}$ was obtained and for each W^{5+} a $Vo^{\bullet}$ was obtained. Therefore, using the data from tables 6 and 7, it is possible to elucidate that the percentages of W^{4+} and W^{5+} also correspond to the percentages $Vo^{\bullet\bullet}$ and $Vo^{\bullet}$, respectively.

Finally, with the percentages of W^{4+} and W^{5+} (obtained from the XPS) and their 1:1 ratio (according to equations 11 and 12), it is possible to calculate the percentage of oxygen vacancies formed in all samples, table 8.

Table 8 Percentage of $V_o^{\bullet}$, $V_o^{\bullet\bullet}$ and total oxygen vacancies in all samples.

Samples	$V_o^{\bullet}$ %	$V_o^{\bullet\bullet}$ %	Total oxygen vacancies %
Ar	14.47	0.7	15.17
AAr300	20.04	4.04	24.08
AAr400	40.36	6.04	46.4
AAr500	35.64	8.3	42.94
AH300	12.27	--	12.27
AH400	25.55	3.17	28.72
AH500	80.03	15.09	95.12

The results of table 8 exhibits the direct relationship of temperature with the generation of oxygen vacancies and confirm, together with the data obtained by the EPR and the red-shift in the starching bands of the Raman spectroscopy, that the highest concentration of oxygen vacancies is related to the samples AH400 and AH500.

5.5
Thermal conductivity

The thermal conductivity at room temperature is 0.15 W m^{-1} K^{-1} for the Ar sample and 0.35 W m^{-1} K^{-1} for the AAr400 sample (Figure 25). The thermal conductivity of the samples is low as expected for the $A_2M_3O_{12}$ family and related families. It is, for example, 1.04 W m^{-1} K^{-1} for $HfMgMo_3O_{12}$ [73], 0.8 W m^{-1} K^{-1} for $Y_2Mo_3O_{12}$ [74] and 0.63 W m^{-1} K^{-1} for $Al_2W_3O_{12}$ [10]. The results demonstrate that the temperature dependence of the thermal conductivity is similar to the amorphous solids.

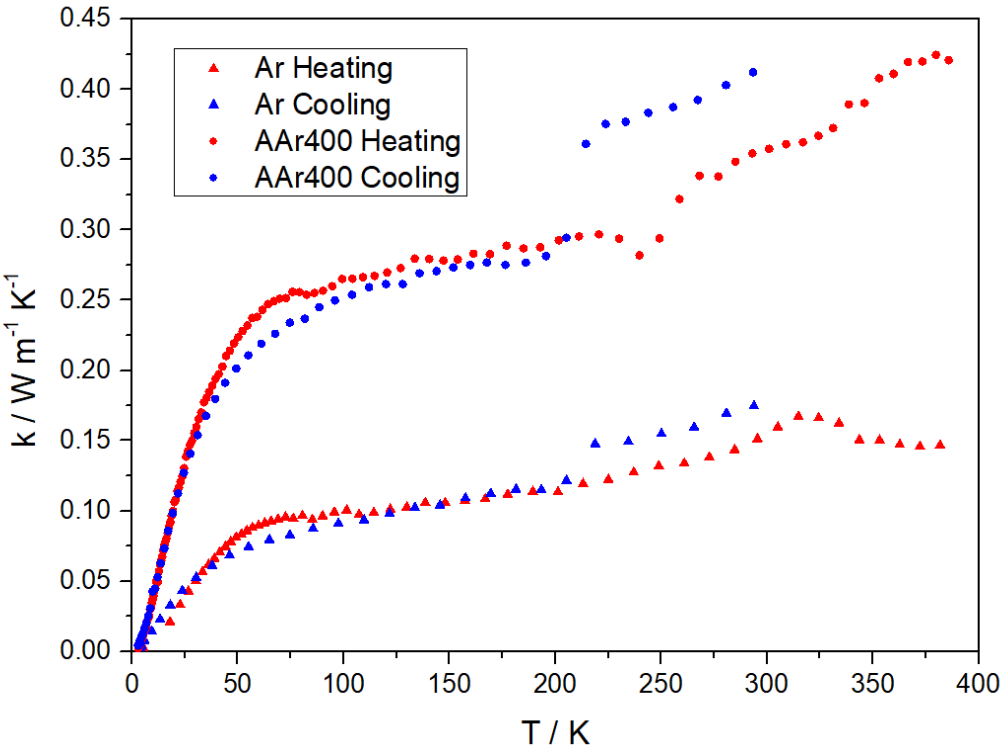

Figure 25 Thermal conductivity of Ar and AAr 400 samples.

6
Conclusions and future works

- The existence of oxygen vacancies in the crystal structure of $Al_2W_3O_{12}$ does not modify the orthorhombic structure.
- Reducing atmosphere (i.e. hydrogen) and inert atmosphere (i.e. argon) manage to produce oxygen vacancies. However, the oxygen vacancies concentration is higher in the samples treated with hydrogen atmospheres.
- The increase in temperature favors the formation of oxygen vacancies. Heat treatments with elevated temperatures indicate higher concentrations of oxygen vacancies.
- The charge compensation in $Al_2W_3O_{12}$ for oxygen vacancies is performed by the formation of lower valance species such as W^{4+} and the increase of the W^{5+}. It is possible to observe that regardless of the heat treatment and atmosphere, the presence of W^{6+} decreases at the highest temperatures, as shown in samples AAr500 and AH500.
- Raman spectroscopy allows indirect identification of oxygen vacancies in the samples treated with hydrogen atmosphere due to the relaxation in the crystal structure generated by the presence of oxygen vacancies. However, it was not possible to identify oxygen vacancies in samples treated with Ar atmospheres.
- EPR spectra were able to identify oxygen vacancies in $Al_2W_3O_{12}$. However, it is advisable to make new measurements with the temperature variation to obtain clearer signals in the spectrum.
- Oxygen vacancies favor the absorption within the UV-vis spectra by forming sublevels in the bandgap.
- Oxygen vacancies allow a reduction in CTE. Higher concentrations of oxygen vacancies favor this behavior.
- The thermal conductivity at room temperature of the samples Ar and AAr400 is between the values corresponding to the family $A_2M_3O_{12}$.

- The operation time was not considered in this study. Therefore, it is suggested a further study in this variable.

7
References

[1] C.P. Romao, K.J. Miller, C.A. Whitman, M.A. White, B.A. Marinkovic, Negative Thermal Expansion (Thermomiotic) Materials, Elsevier Ltd., 2013. https://doi.org/10.1016/B978-0-08-097774-4.00425-3.

[2] K.J. Miller, C.P. Romao, M. Bieringer, B.A. Marinkovic, L. Prisco, M.A. White, Near-zero thermal expansion in in (HfMg)0.5Mo3O 12, Journal of the American Ceramic Society. 96 (2013) 561–566. https://doi.org/10.1111/jace.12085.

[3] X. Lu, Y. Zeng, M. Yu, T. Zhai, C. Liang, S. Xie, M.S. Balogun, Y. Tong, Oxygen-deficient hematite nanorods as high-performance and novel negative electrodes for flexible asymmetric supercapacitors, Advanced Materials. 26 (2014) 3148–3155. https://doi.org/10.1002/adma.201305851.

[4] Q. Liu, F. Wang, H. Lin, Y. Xie, N. Tong, J. Lin, X. Zhang, Z. Zhang, X. Wang, Surface oxygen vacancy and defect engineering of WO3 for improved visible light photocatalytic performance, Catalysis Science and Technology. 8 (2018) 4399–4406. https://doi.org/10.1039/c8cy00994e.

[5] Y. Cheng, Y. Mao, B. Yuan, X. Ge, J. Guo, M. Chao, E. Liang, Enhanced negative thermal expansion and optical absorption of In0.6(HfMg)0.7Mo3O12 with oxygen vacancies, Physics Letters, Section A: General, Atomic and Solid State Physics. 381 (2017) 2195–2199. https://doi.org/10.1016/j.physleta.2017.05.002.

[6] Y. Cheng, Y. Mao, B. Yuan, X. Ge, J. Guo, M. Chao, E. Liang, Enhanced negative thermal expansion and optical absorption of In0.6(HfMg)0.7Mo3O12 with oxygen vacancies, Physics Letters, Section A: General, Atomic and Solid State Physics. 381 (2017) 2195–2199. https://doi.org/10.1016/j.physleta.2017.05.002.

[7] W. Miller, C.W. Smith, D.S. MacKenzie, K.E. Evans, Negative thermal expansion: A review, Journal of Materials Science. 44 (2009) 5441–5451. https://doi.org/10.1007/s10853-009-3692-4.

[8] P.J. Attfield, Mechanisms and materials for NTE, Frontiers in Chemistry. 6 (2018) 1–6. https://doi.org/10.3389/fchem.2018.00371.

[9] H. Liu, W. Sun, Z. Zhang, L. Lovings, C. Lind, Thermal Expansion Behavior in the A2M3O12 Family of Materials, Solids. 2 (2021) 87–107. https://doi.org/10.3390/solids2010005.

[10] B.A. Marinkovic, P.I. Pontón, C.P. Romao, T. Moreira, M.A. White, Negative and Near-Zero Thermal Expansion in A2M3O12 and Related Ceramic Families: A Review, Frontiers in Materials. 8 (2021). https://doi.org/10.3389/fmats.2021.741560.

[11] D.A. Woodcock, P. Lightfoot, C. Ritter, Negative thermal expansion in Y2(WO4)3, Journal of Solid State Chemistry. 149 (2000) 92–98. https://doi.org/10.1006/jssc.1999.8502.

[12] S. Sumithra, A.M. Umarji, Hygroscopicity and bulk thermal expansion in Y2W 3O12, Materials Research Bulletin. 40 (2005) 167–176. https://doi.org/10.1016/j.materresbull.2004.09.009.

[13] H. Liu, W. Sun, Z. Zhang, M. Zhou, X. Meng, X. Zeng, Tailorable thermal expansion and hygroscopic properties of cerium-substituted Y2W3O12 ceramics, Journal of Alloys and Compounds. 751 (2018) 49–55. https://doi.org/10.1016/j.jallcom.2018.04.081.

[14] T. Varga, A.P. Wilkinson, C. Lind, W.A. Bassett, C.S. Zha, High pressure synchrotron x-ray powder diffraction study of Sc 2Mo3O12 and Al2W3O 12, Journal of Physics Condensed Matter. 17 (2005) 4271–4283. https://doi.org/10.1088/0953-8984/17/27/004.

[15] S. Mirsadeghi, H. Zandavar, M. Rahimi, H.F. Tooski, H.R. Rajabi, M. Rahimi-Nasrabadi, E. Sohouli, B. Larijani, S.M. Pourmortazavi, Photocatalytic reduction of imatinib mesylate and imipenem on electrochemical synthesized Al2W3O12 nanoparticle: Optimization, investigation of electrocatalytic and antimicrobial activity, Colloids and Surfaces A: Physicochemical and Engineering Aspects. 586 (2020) 124254. https://doi.org/10.1016/j.colsurfa.2019.124254.

[16] L.P. Prisco, P.I. Pontón, M. V. Guamán, R.R. Avillez, C.P. Romao, M.B. Johnson, M.A. White, B.A. Marinkovic, Assessment of the Thermal Shock Resistance Figures of Merit of Al2W3O12, a Low Thermal Expansion

Ceramic, Journal of the American Ceramic Society. 99 (2016) 1742–1748. https://doi.org/10.1111/jace.14160.

[17] P.I. Pontón, L.P. Prisco, B.A. Marinkovic, Effects of low contents of A2M3O12 submicronic thermomiotic-like fillers on thermal expansion and mechanical properties of HDPE-based composites, Polymer Composites. 39 (2018) E1821–E1833. https://doi.org/10.1002/pc.24811.

[18] P.M. Jardim, E.S. Garcia, B.A. Marinkovic, Young's modulus, hardness and thermal expansion of sintered Al2W3O12 with different porosity fractions, Ceramics International. 42 (2016) 5211–5217. https://doi.org/10.1016/j.ceramint.2015.12.045.

[19] N. Imanaka, M. Hiraiwa, G. Adachi, H. Dabkowska, A. Dabkowski, Thermal contraction behavior in Al2(WO4)3 single crystal, Journal of Crystal Growth. 220 (2000) 176–179. https://doi.org/10.1016/S0022-0248(00)00771-5.

[20] L.P. Prisco, M. Marzano, P.I. Pontón, A.M.L.M. Costa, C.A. da Costa Neto, G. Sweet, C.P. Romao, M.A. White, B.A. Marinkovic, Relationship between sintering methods and physical properties of the low positive thermal expansion material Al2W3O12, International Journal of Applied Ceramic Technology. 16 (2019) 346–356. https://doi.org/10.1111/ijac.13054.

[21] I.M. Costa, V.L. Blair, W. Paraguassu, B.A. Marinkovic, Evaluating Al2-xGaxW3O12 system for thermal shock resistance, Journal of Solid State Chemistry. 277 (2019) 149–158. https://doi.org/10.1016/j.jssc.2019.05.041.

[22] I. Yanase, R. Ootomo, H. Kobayashi, Effect of B substitution on thermal changes of UV–Vis and Raman spectra and color of Al2W3O12 powder, Journal of Thermal Analysis and Calorimetry. 132 (2018). https://doi.org/10.1007/s10973-017-6933-9.

[23] N. Dasgupta, E. Sörge, B. Butler, T.C. Wen, D.K. Shetty, L.R. Cambrea, D.C. Harris, Synthesis and characterization of Al 2-xSc x(WO 4) 3 ceramics for low-expansion infrared-transmitting windows, Journal of Materials Science. 47 (2012) 6286–6296. https://doi.org/10.1007/s10853-012-6548-2.

[24] B.A. Cerón Cortés, A.E. Marinkovic, Phase Transition and Coefficients of Thermal Expansion in Al2-xInxW3O12, Materials. 12 (2021). https://doi.org/https://doi.org/10.3390/ma14144021.

[25] A. Surjith, N.K. James, R. Ratheesh, Synthesis, structural and microwave dielectric properties of Al 2W3-xMoxO12 (x = 0-3) ceramics, Journal of Alloys and Compounds. 509 (2011) 9992–9995. https://doi.org/10.1016/j.jallcom.2011.08.007.

[26] B. Schulz, H.L. Andersen, O.K. Al Bahri, B. Johannessen, J. Liu, S. Primig, N. Sharma, Electrochemical performance and structure of Al2W3-: XMoxO12, CrystEngComm. 20 (2018) 1352–1360. https://doi.org/10.1039/c7ce01707c.

[27] H.L. Tuller, S.R. Bishop, Point defects in oxides: Tailoring materials through defect engineering, Annual Review of Materials Research. 41 (2011) 369–398. https://doi.org/10.1146/annurev-matsci-062910-100442.

[28] M.A. White, Physical properties of materials, 2018. https://doi.org/10.1007/978-3-319-73845-1_2.

[29] G. Li, G.R. Blake, T.T.M. Palstra, Vacancies in functional materials for clean energy storage and harvesting: The perfect imperfection, Chemical Society Reviews. 46 (2017) 1693–1706. https://doi.org/10.1039/c6cs00571c.

[30] P. Rudolph, Fundamentals and engineering of defects, Progress in Crystal Growth and Characterization of Materials. 62 (2016) 89–110. https://doi.org/10.1016/j.pcrysgrow.2016.04.004.

[31] F. Banhart, J. Kotakoski, A. v. Krasheninnikov, Structural defects in graphene, ACS Nano. 5 (2011) 26–41. https://doi.org/10.1021/nn102598m.

[32] Y. Wang, X. Xiao, Q. Li, H. Pang, Synthesis and Progress of New Oxygen-Vacant Electrode Materials for High-Energy Rechargeable Battery Applications, Small. 14 (2018) 1–23. https://doi.org/10.1002/smll.201802193.

[33] M. Zhao, W. Pan, C. Wan, Z. Qu, Z. Li, J. Yang, Defect engineering in development of low thermal conductivity materials: A review, Journal of the European Ceramic Society. 37 (2017) 1–13. https://doi.org/10.1016/j.jeurceramsoc.2016.07.036.

[34] C.B.C.M.G. Norton, Ceramic materials: science and engineering, New York, 2007.

[35] H. xia TONG, Q. yuan CHEN, Z. lan YIN, H. ping HU, D. xin WU, Y. hui YANG, Preparation, characterization and photo-catalytic behavior of WO3-TiO2 catalysts with oxygen vacancies, Transactions of Nonferrous Metals

Society of China (English Edition). 19 (2009) 1483–1488. https://doi.org/10.1016/S1003-6326(09)60056-X.

[36] A. Kotlov, S. Dolgov, E. Feldbach, L. Jönsson, M. Kirm, A. Lushchik, V. Nagirnyi, G. Svensson, B.I. Zadneprovski, Exciton and recombination luminescence of Al2(WO 4)3 crystals, Physica Status Solidi C: Conferences. 2 (2005) 61–64. https://doi.org/10.1002/pssc.200460111.

[37] C. Zhang, G. Liu, X. Geng, K. Wu, M. Debliquy, Metal oxide semiconductors with highly concentrated oxygen vacancies for gas sensing materials: A review, Sensors and Actuators, A: Physical. 309 (2020) 112026. https://doi.org/10.1016/j.sna.2020.112026.

[38] C. Drouilly, J.M. Krafft, F. Averseng, S. Casale, D. Bazer-Bachi, C. Chizallet, V. Lecocq, H. Vezin, H. Lauron-Pernot, G. Costentin, ZnO oxygen vacancies formation and filling followed by in situ photoluminescence and in situ EPR, Journal of Physical Chemistry C. 116 (2012) 21297–21307. https://doi.org/10.1021/jp307693y.

[39] Q. Ji, L. Bi, J. Zhang, H. Cao, X.S. Zhao, The role of oxygen vacancies of ABO3perovskite oxides in the oxygen reduction reaction, Energy and Environmental Science. 13 (2020) 1408–1428. https://doi.org/10.1039/d0ee00092b.

[40] J.T. Mefford, X. Rong, A.M. Abakumov, W.G. Hardin, S. Dai, A.M. Kolpak, K.P. Johnston, K.J. Stevenson, Water electrolysis on La1-xSrxCoO3-δ perovskite electrocatalysts, Nature Communications. 7 (2016). https://doi.org/10.1038/ncomms11053.

[41] S. Chen, Y. Xiao, Y. Wang, Z. Hu, H. Zhao, W. Xie, A facile approach to prepare black TiO2 with oxygen vacancy for enhancing photocatalytic activity, Nanomaterials. 8 (2018) 1–16. https://doi.org/10.3390/nano8040245.

[42] S. Ubenthiran, S. Ramesh, C.Y. Tan, W.D. Teng, Oxygen vacancy comparisons for 3Y - TZP sintered in air and argon gas atmosphere, Applied Mechanics and Materials. 372 (2013) 173–176. https://doi.org/10.4028/www.scientific.net/AMM.372.173.

[43] G. Wang, Y. Yang, Y. Ling, H. Wang, X. Lu, Y.C. Pu, J.Z. Zhang, Y. Tong, Y. Li, An electrochemical method to enhance the performance of metal

oxides for photoelectrochemical water oxidation, Journal of Materials Chemistry A. 4 (2016) 2849–2855. https://doi.org/10.1039/c5ta10477g.

[44] D.C. Harris, Optical Properties of Infrared Windows, 2010. https://doi.org/10.1117/3.349896.ch2.

[45] A. Naldoni, M. Allieta, S. Santangelo, M. Marelli, F. Fabbri, S. Cappelli, C.L. Bianchi, R. Psaro, V. Dal Santo, Effect of nature and location of defects on bandgap narrowing in black TiO 2 nanoparticles, Journal of the American Chemical Society. 134 (2012) 7600–7603. https://doi.org/10.1021/ja3012676.

[46] S. Chen, Y. Xiao, Y. Wang, Z. Hu, H. Zhao, W. Xie, A facile approach to prepare black TiO2 with oxygen vacancy for enhancing photocatalytic activity, Nanomaterials. 8 (2018) 1–16. https://doi.org/10.3390/nano8040245.

[47] Y. Lv, W. Yao, R. Zong, Y. Zhu, Fabrication of wide-range-visible photocatalyst Bi2WO6-x nanoplates via surface oxygen vacancies, Scientific Reports. 6 (2016) 1–9. https://doi.org/10.1038/srep19347.

[48] N. Burger, A. Laachachi, M. Ferriol, M. Lutz, V. Toniazzo, D. Ruch, Review of thermal conductivity in composites: Mechanisms, parameters and theory, Progress in Polymer Science. 61 (2016) 1–28. https://doi.org/10.1016/j.progpolymsci.2016.05.001.

[49] S. Ning, S.C. Huberman, Z. Ding, H.H. Nahm, Y.H. Kim, H.S. Kim, G. Chen, C.A. Ross, Anomalous Defect Dependence of Thermal Conductivity in Epitaxial WO3 Thin Films, Advanced Materials. 31 (2019) 1–8. https://doi.org/10.1002/adma.201903738.

[50] P.G. Klemens, Phonon scattering by oxygen vacancies in ceramics, Physica B: Condensed Matter. 263–264 (1999) 102–104. https://doi.org/10.1016/S0921-4526(98)01202-2.

[51] Z. Qu, T.D. Sparks, W. Pan, D.R. Clarke, Thermal conductivity of the gadolinium calcium silicate apatites: Effect of different point defect types, Acta Materialia. 59 (2011) 3841–3850. https://doi.org/10.1016/j.actamat.2011.03.008.

[52] J.U. Rahman, W.H. Nam, N. Van Du, G. Rahman, A.U. Rahman, W.H. Shin, W.S. Seo, M.H. Kim, S. Lee, Oxygen vacancy revived phonon-glass

electron-crystal in SrTiO3, Journal of the European Ceramic Society. 39 (2019) 358–365. https://doi.org/10.1016/j.jeurceramsoc.2018.09.036.

[53] Б.А. Струков, А.П. Леванюк, The optical absorption edge of rare earth sesquisulfides and alkaline earth - rare earth sulfides, 18 (1983) 240.

[54] T. Tauc, P. Kubelka, F. Munk, S. Information, T. Tauc, How To Correctly Determine the Band Gap Energy of Modi fi ed Semiconductor Photocatalysts Based on UV − Vis Spectra, (2018) 8–11. https://doi.org/10.1021/acs.jpclett.8b02892.

[55] M. Habran, P.I. Pontón, L. Mancic, O. Pandoli, K. Krambrock, M.E.H.M. da Costa, S. Letichevsky, A.M.L.M. Costa, E. Morgado, B.A. Marinkovic, Visible light sensitive mesoporous nanohybrids of lepidocrocite-like ferrititanate coupled to a charge transfer complex: Synthesis, characterization and photocatalytic degradation of NO, Journal of Photochemistry and Photobiology A: Chemistry. 365 (2018) 133–144. https://doi.org/10.1016/j.jphotochem.2018.07.038.

[56] W. Wang, C.H. Lu, Y.R. Ni, J. bin Song, M.X. Su, Z.Z. Xu, Enhanced visible-light photoactivity of {001} facets dominated TiO 2 nanosheets with even distributed bulk oxygen vacancy and Ti 3+, Catalysis Communications. 22 (2012) 19–23. https://doi.org/10.1016/j.catcom.2012.02.011.

[57] S. Xu, Y. Hu, Y. Liang, C. Shi, Y. Su, J. Guo, Q. Gao, M. Chao, E. Liang, Negative thermal expansion of Ca2RuO4with oxygen vacancies, Chinese Physics B. 29 (2020). https://doi.org/10.1088/1674-1056/ab8a36.

[58] Y. Hu, X. Liu, S. Xu, W. Wei, G. Zeng, H. Yuan, Q. Gao, J. Guo, M. Chao, E. Liang, Improving the Thermal Expansion and Capacitance Properties of MoO3by Introducing Oxygen Vacancies, Journal of Physical Chemistry C. 125 (2021) 10817–10823. https://doi.org/10.1021/acs.jpcc.1c02405.

[59] N. Zhang, W. Zhou, M. Chao, Y. Mao, J. Guo, Y. Li, D. Feng, E. Liang, Negative thermal expansion, optical and electrical properties of HfMnMo2PO12-δ, Ceramics International. 41 (2015) 15170–15175. https://doi.org/10.1016/j.ceramint.2015.08.090.

[60] S.S. Kalanur, I.H. Yoo, I.S. Cho, H. Seo, Effect of oxygen vacancies on the band edge properties of WO3 producing enhanced photocurrents, Electrochimica Acta. 296 (2019) 517–527. https://doi.org/10.1016/j.electacta.2018.11.061.

[61] A.J. Deotale, R. V. Nandedkar, Correlation between Particle Size, Strain and Band Gap of Iron Oxide Nanoparticles, Materials Today: Proceedings. 3 (2016) 2069–2076. https://doi.org/10.1016/j.matpr.2016.04.110.

[62] M. Habran, P.I. Pontón, L. Mancic, O. Pandoli, K. Krambrock, M.E.H.M. da Costa, S. Letichevsky, A.M.L.M. Costa, E. Morgado, B.A. Marinkovic, Visible light sensitive mesoporous nanohybrids of lepidocrocite-like ferrititanate coupled to a charge transfer complex: Synthesis, characterization and photocatalytic degradation of NO, Journal of Photochemistry and Photobiology A: Chemistry. 365 (2018) 133–144. https://doi.org/10.1016/j.jphotochem.2018.07.038.

[63] A. Ajmi, K. Karoui, K. Khirouni, A. ben Rhaiem, Optical and dielectric properties of NaCoPO4 in the three phases α, β and γ, RSC Advances. 9 (2019) 14772–14781. https://doi.org/10.1039/c9ra01558b.

[64] B. Choudhury, A. Choudhury, Oxygen defect dependent variation of band gap, Urbach energy and luminescence property of anatase, anatase-rutile mixed phase and of rutile phases of TiO2 nanoparticles, Physica E: Low-Dimensional Systems and Nanostructures. 56 (2014) 364–371. https://doi.org/10.1016/j.physe.2013.10.014.

[65] F. Mehmood, J. Iqbal, T. Jan, W. Ahmed, W. Ahmed, A. Arshad, Q. Mansoor, S.Z. Ilyas, M. Ismail, I. Ahmad, Effect of Sn doping on the structural, optical, electrical and anticancer properties of WO3 nanoplates, Ceramics International. 42 (2016) 14334–14341. https://doi.org/10.1016/j.ceramint.2016.04.010.

[66] W. Paraguassu, M. Maczka, A.G.S. Filho, P.T.C. Freire, F.E.A. Melo, J.M. Filho, J. Hanuza, A comparative study of negative thermal expansion materials Sc2(MoO4)3 and Al2(WO4)3 crystals, Vibrational Spectroscopy. 44 (2007) 69–77. https://doi.org/10.1016/j.vibspec.2006.08.006.

[67] M. Guo, J. Lu, Y. Wu, Y. Wang, M. Luo, UV and visible Raman studies of oxygen vacancies in rare-earth-doped ceria, Langmuir. 27 (2011) 3872–3877. https://doi.org/10.1021/la200292f.

[68] F.D. Brandão, M.V.B. Pinheiro, G.M. Ribeiro, G. Medeiros-Ribeiro, K. Krambrock, Identification of two light-induced charge states of the oxygen vacancy in single-crystalline rutile TiO2, Physical Review B - Condensed

Matter and Materials Physics. 80 (2009) 1–7. https://doi.org/10.1103/PhysRevB.80.235204.

[69] Z. Li, W. Yang, L. Xie, Y. Li, Y. Liu, Y. Sun, Y. Bu, X. Mi, S. Zhan, W. Hu, Prominent role of oxygen vacancy for superoxide radical and hydroxyl radical formation to promote electro-Fenton like reaction by W-doped CeO2 composites, Applied Surface Science. 549 (2021) 1–11. https://doi.org/10.1016/j.apsusc.2021.149262.

[70] B. Sarwan, B. Pare, A.D. Acharya, The effect of oxygen vacancies on the photocatalytic activity of BiOCl nanocrystals prepared by hydrolysis and UV light irradiation, Materials Science in Semiconductor Processing. 25 (2014) 89–97. https://doi.org/10.1016/j.mssp.2013.09.015.

[71] J.M. Cho, W.J. Yun, J.K. Lee, H.S. Lee, W.W. So, S.J. Moon, Y. Jia, H. Kulkarni, Y. Wu, Electron spin resonance from annealed titania nanotubes, Applied Physics A: Materials Science and Processing. 88 (2007) 751–755. https://doi.org/10.1007/s00339-007-4063-0.

[72] V.B. Kumar, D. Mohanta, Probing spin-spin and spin-lattice relaxation through electron paramagnetic resonance study of nanoscale WO3-x system, Materials Express. 2 (2012) 57–63. https://doi.org/10.1166/mex.2012.1048.

[73] K.J. Miller, M.B. Johnson, M.A. White, B.A. Marinkovic, Low-temperature investigations of the open-framework material HfMgMo 3O 12, Solid State Communications. 152 (2012) 1748–1752. https://doi.org/10.1016/j.ssc.2012.06.022.

[74] C.P. Romao, K.J. Miller, M.B. Johnson, J.W. Zwanziger, B.A. Marinkovic, M.A. White, Thermal, vibrational, and thermoelastic properties of Y2 Mo3 O12 and their relations to negative thermal expansion, Physical Review B - Condensed Matter and Materials Physics. 90 (2014) 1–9. https://doi.org/10.1103/PhysRevB.90.024305.

Appedix A: Supplementary material to support section 5.1

A.1

Natural logarithmic variations of unit-cell parameters (a, b and c) and unit-cell volume as function of temperature.

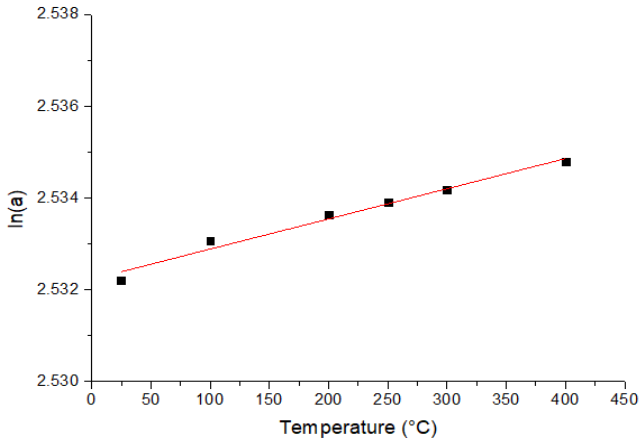

(a)

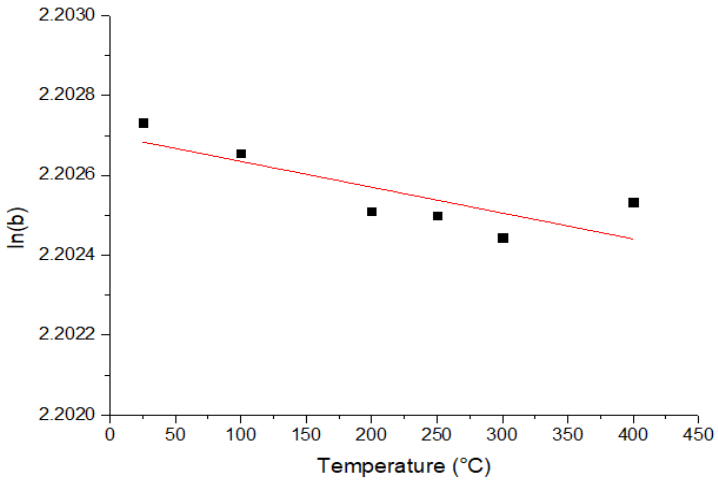

(b)

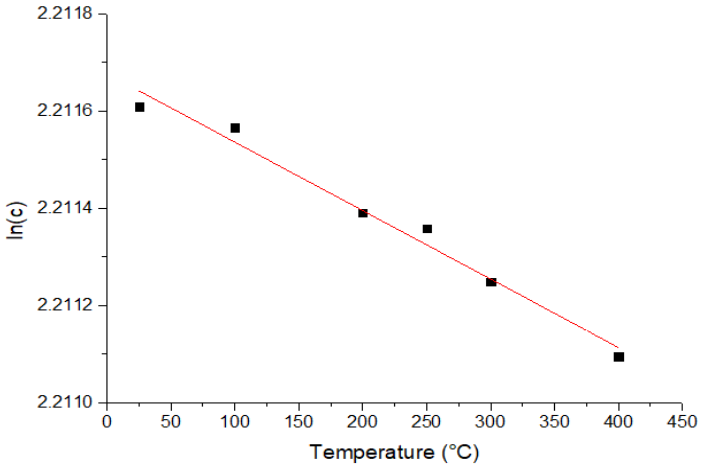

(c)

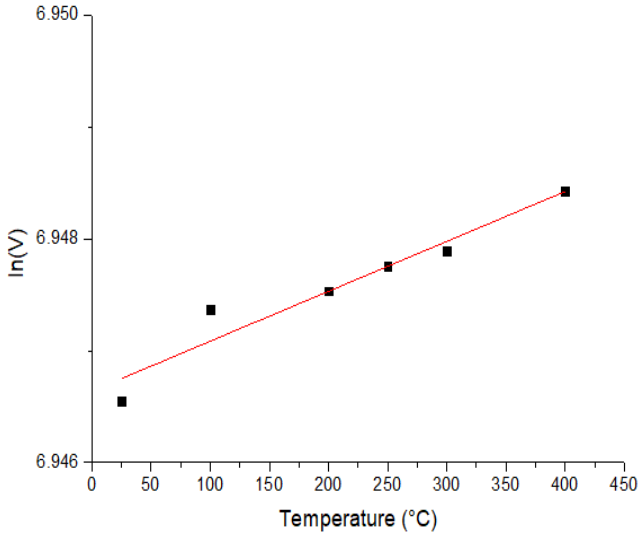

(d)

Figure A1.1- Natural logarithmic variations of unit-cell parameters (a, b and c) and unit-cell volume (d) as function of temperature for Ar sample.

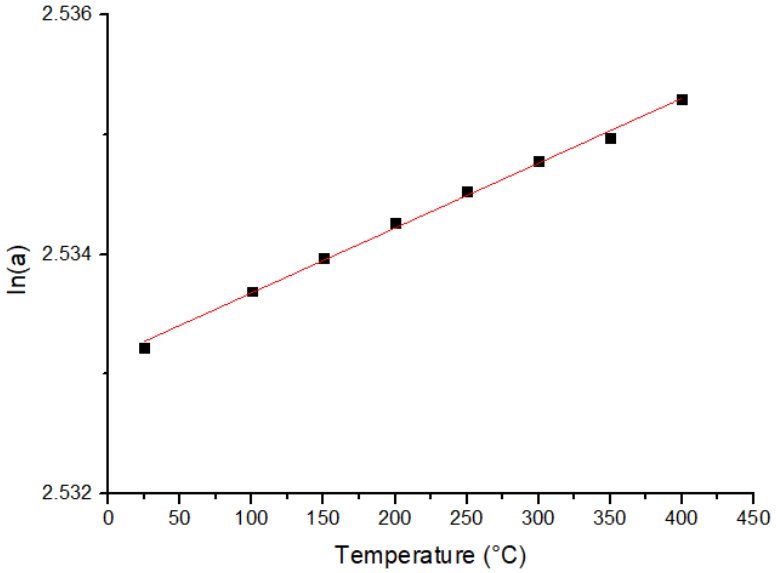

(a)

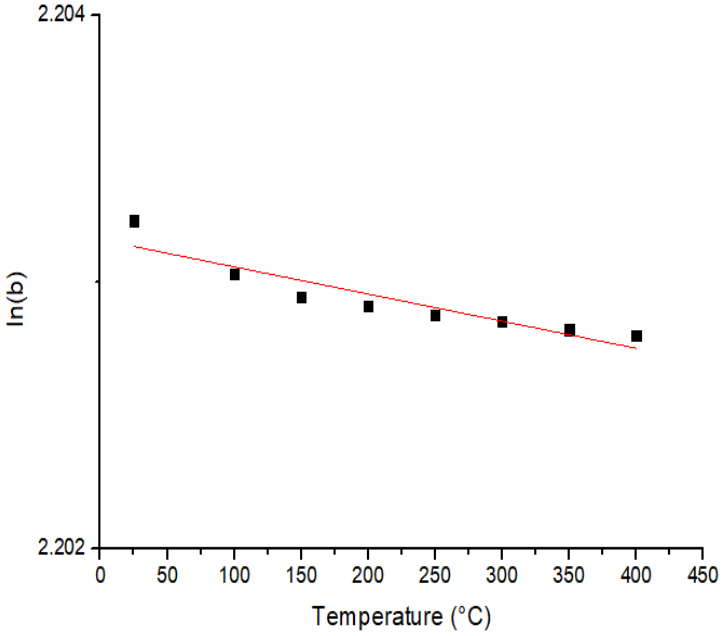

(b)

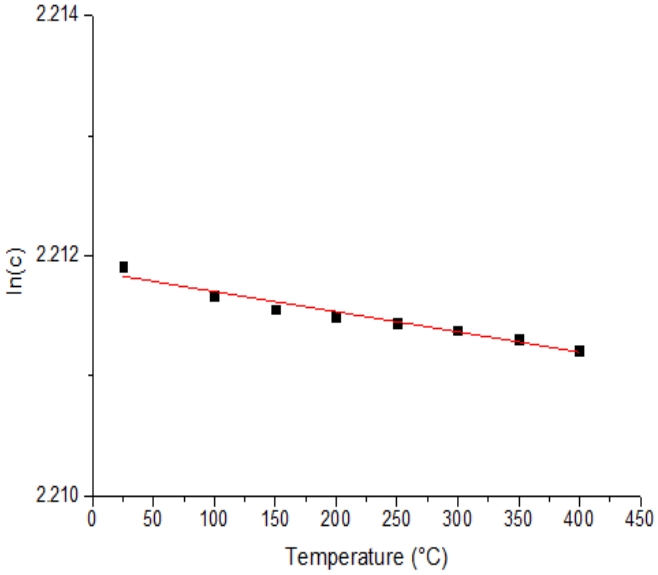

(c)

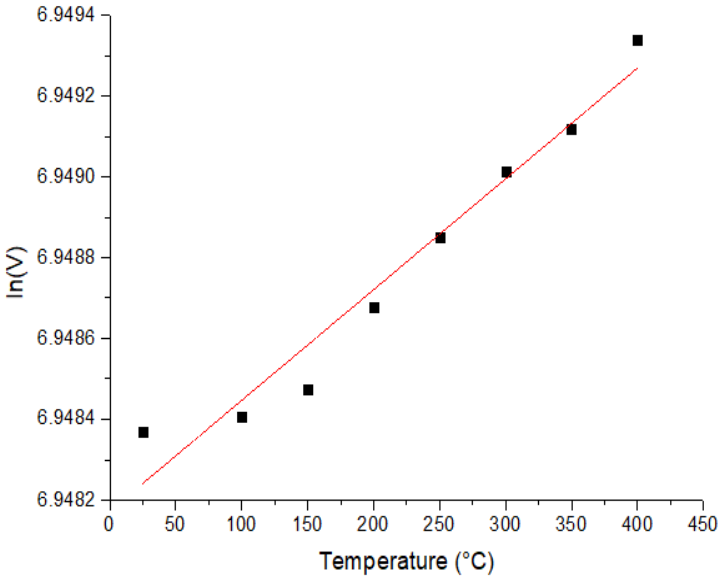

(d)

Figure A1.2- Natural logarithmic variations of unit-cell parameters (a, b and c) and unit-cell volume (d) as function of temperature for AH400 sample.

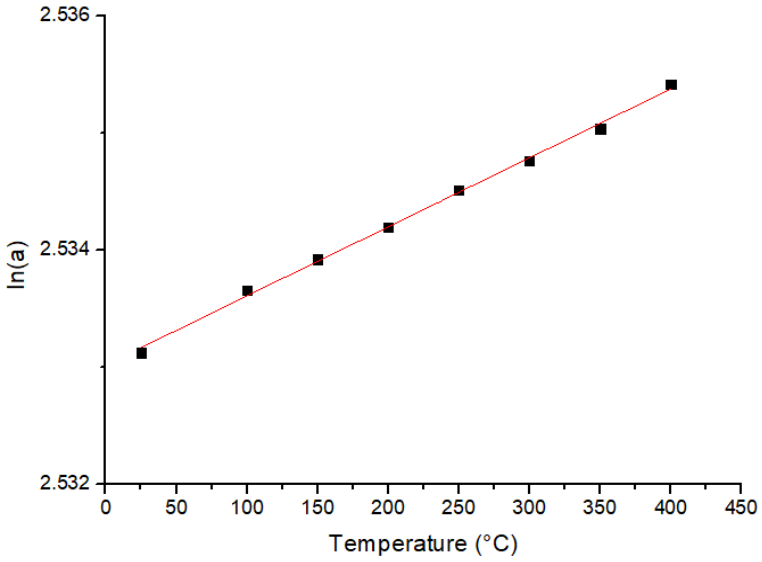

(a)

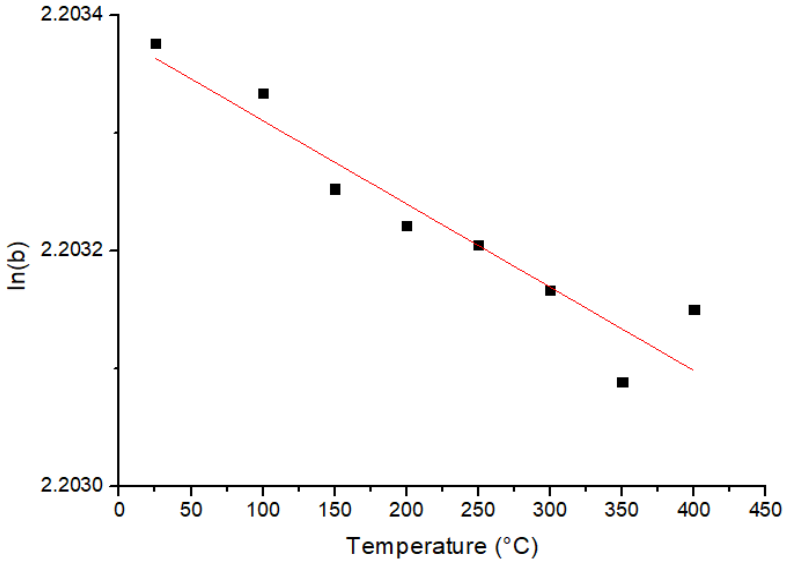

(b)

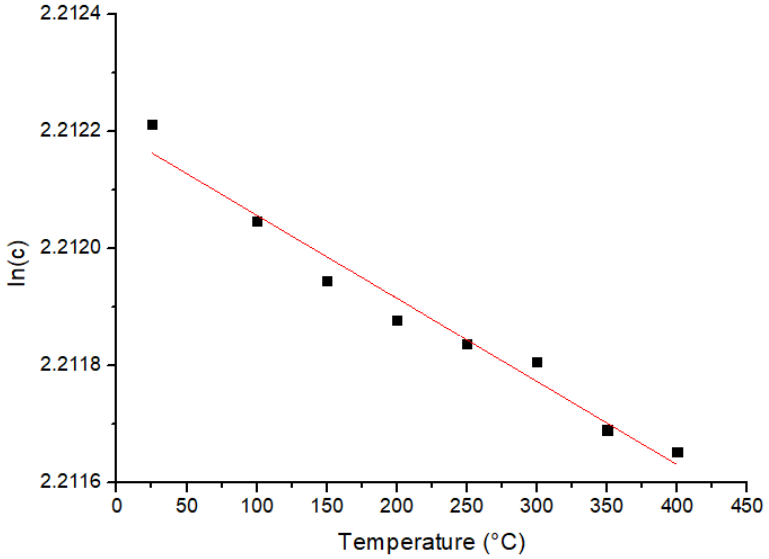

(c)

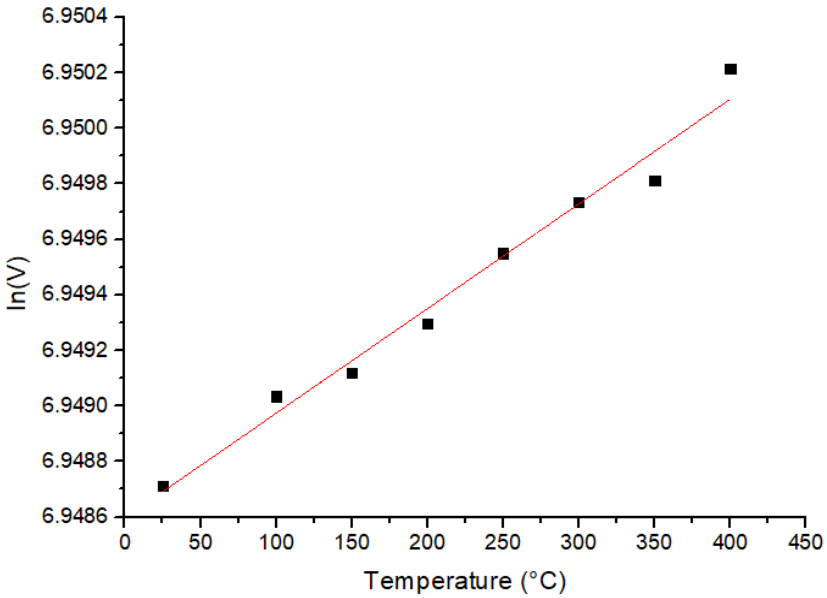

(d)

Figure A1.3- Natural logarithmic variations of unit-cell parameters (a, b and c) and unit-cell volume (d) as function of temperature for AAr400 sample.

A.2

Area of peaks 14° and 15 °

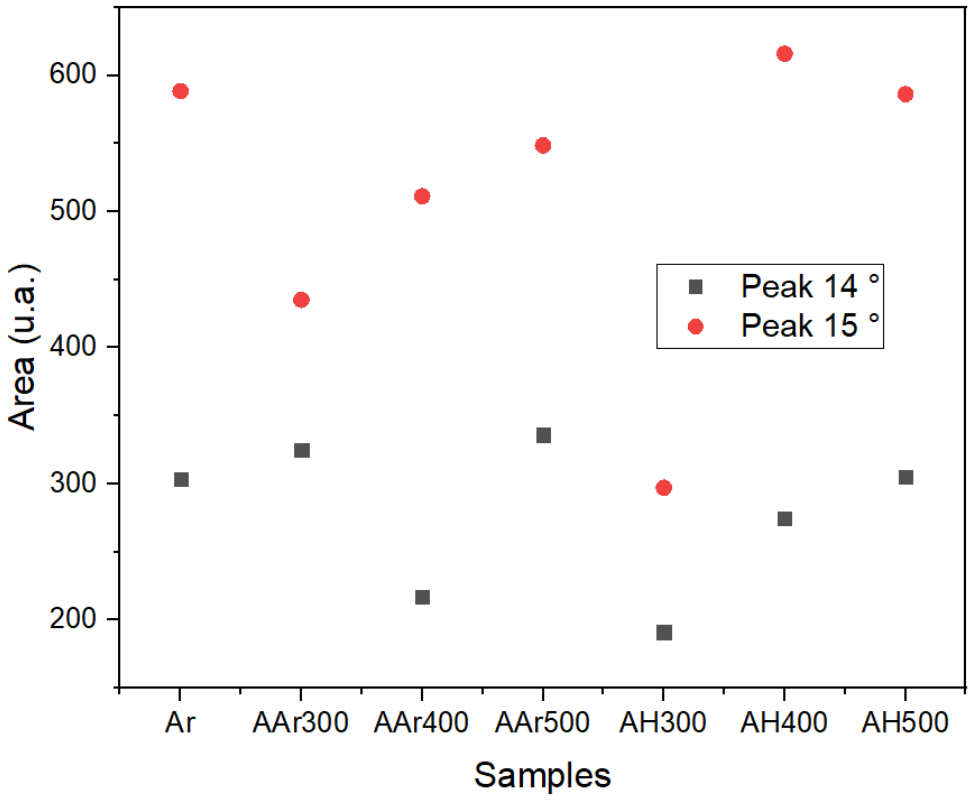

Figure A2.1- Area of peaks 14° and 15 °.

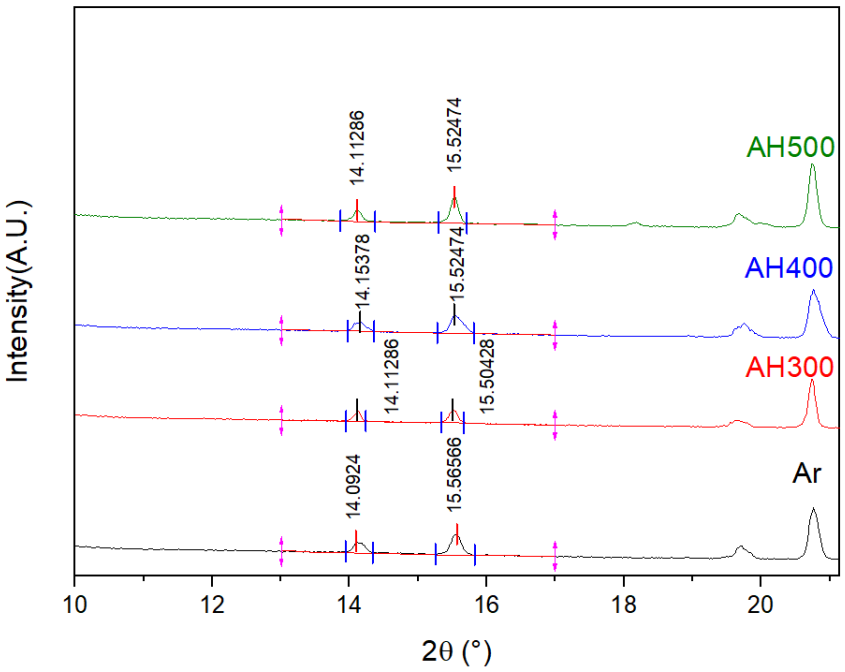

(a)

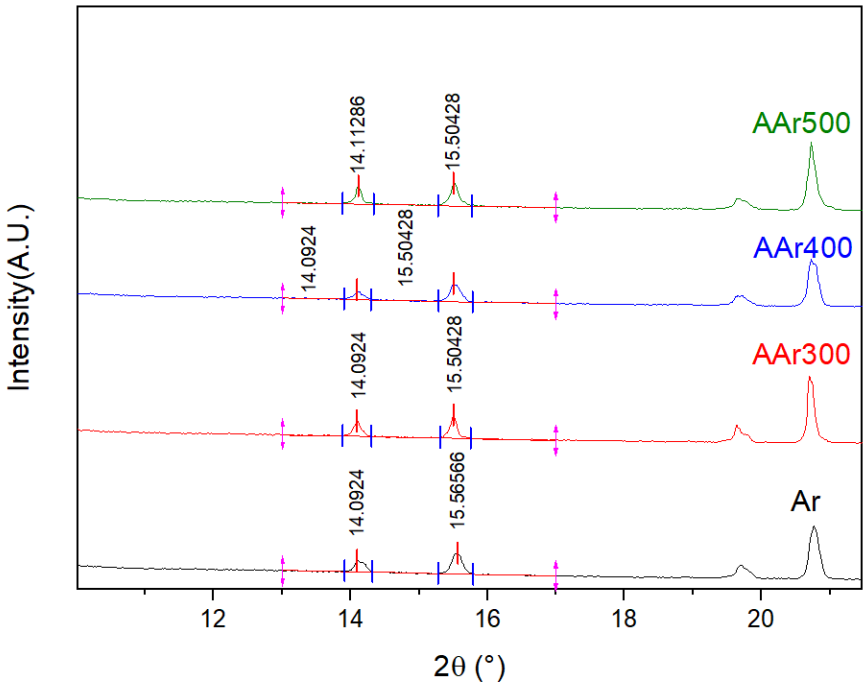

(b)

Figure A2.1- localitation of peaks 14° and 15° in the AH300, AH400, AH500 (a), Aar300, Aar400,Aar500 (b) and Ar samples.

Appedix B: Supplementary material to support section 5.2

B.1

Urban energy calculations

$$SamplesAr: E_u = \frac{1}{slope} = \frac{1}{8.56017805} = 0{,}11682\ eV = 116{,}82\ meV$$

$$SamplesAAr300: E_u = \frac{1}{slope} = \frac{1}{4.95441934} = 0.20184\ eV = 201.84\ meV$$

$$SamplesAAr400: E_u = \frac{1}{slope} = \frac{1}{6.20462865} = 0{,}11682\ eV = 161.17\ meV$$

$$SamplesAAr500: E_u = \frac{1}{slope} = \frac{1}{5.55031359} = 0.18017\ eV = 180.17\ meV$$

$$SamplesAH300: E_u = \frac{1}{slope} = \frac{1}{4.44010301} = 0.22522\ eV = 225.22\ meV$$

$$SamplesAH400: E_u = \frac{1}{slope} = \frac{1}{1.16695646} = 0.85693\ eV = 856.93 meV$$